

A TRIDENT SCHOLAR PROJECT REPORT

NO. 253

OPTIMIZATION OF THE PHOTON RESPONSE FOR A LIF
THERMOLUMINESCENT DOSIMETER



UNITED STATES NAVAL ACADEMY
ANNAPOLIS, MARYLAND

This document has been approved for public
release and sale; its distribution is unlimited.

19990121 140

REPORT DOCUMENTATION PAGE

Form Approved
OMB no. 0704-0188

Public reporting burden for this collection of information is estimated to average 1 hour of response, including the time for reviewing instructions, searching existing data sources, gathering and maintaining the data needed, and completing and reviewing the collection of information. Send comments regarding this burden estimate or any other aspect of the collection of information, including suggestions for reducing this burden, to Washington Headquarters Services, Directorate for Information Operations and Reports, 1215 Jefferson

1. AGENCY USE ONLY (Leave blank)		2. REPORT DATE	3. REPORT TYPE AND DATES COVERED	
4. TITLE AND SUBTITLE Optimization of the photon response for a LiF thermoluminescent dosimeter			5. FUNDING NUMBERS	
6. AUTHOR(S) Robert C. Carnell				
7. PERFORMING ORGANIZATIONS NAME(S) AND ADDRESS(ES) U.S. Naval Academy, Annapolis, MD			8. PERFORMING ORGANIZATION REPORT NUMBER USNA Trident report; no. 253 (1998)	
9. SPONSORING/MONITORING AGENCY NAME(S) AND ADDRESS(ES)			10. SPONSORING/MONITORING AGENCY REPORT NUMBER	
11. SUPPLEMENTARY NOTES Accepted by the U.S. Trident Scholar Committee				
12a. DISTRIBUTION/AVAILABILITY STATEMENT This document has been approved for public release; its distribution is UNLIMITED.			12b. DISTRIBUTION CODE	
13. ABSTRACT (Maximum 200 words) A Harshaw LiF TLD card holder was optimized for maximum discrimination between different energies of irradiating photons in order to improve the dosimetric response. Since dose is proportional energy deposited, a theoretical model was created to estimate the TLD response by calculating the energy deposition. These results correlated with experimental data from NIST to within 20%. In order to increase the accuracy of the model, energy deposition calculations were made using the MCNP particle transport program. MCNP improved the correlation of the modeled data with the experimental data. Next, Harshaw's 8825 card holder was optimized for photon energy determination by analyzing the card holder's response with different filter materials and thickness. This analysis showed that increasing the copper filter thickness by 20 times and doubling the tin filter thickness compared to the original 8825 design improved the TLD's photon energy determination response. The improved 8825 card holder was constructed and experiments were conducted at Armstrong Laboratories. The MCNP model predicted the experimental response of the card holder to within two standard deviations for all beams except M60. Finally, recommendations for a new card holder were made by Naval Dosimetry Center which included a modified filter for improved dose determination.				
14. SUBJECT TERMS Thermoluminescent dosimeter, Monte Carlo, Radiation transport			15. NUMBER OF PAGES	
			16. PRICE CODE	
17. SECURITY CLASSIFICATION OF REPORT	18. SECURITY CLASSIFICATION THIS PAGE	19. SECURITY CLASSIFICATION OF ABSTRACT	20. LIMITATION OF ABSTRACT	

U.S.N.A.---Trident Scholar project report; no. 253 (1998)

Optimization of the Photon Response for a LiF
Thermoluminescent Dosimeter

by

Midshipman Robert C. Carnell, Class of 1998
United States Naval Academy
Annapolis, Maryland



(signature)

Certification of Adviser Approval

Professor Martin E. Nelson
Department of Naval Architecture, Ocean, and Marine
Engineering



(signature)

4/28/98

(date)

Acceptance for the Trident Scholar Committee

Professor Joyce E. Shade
Chair, Trident Scholar Committee



(signature)

4/29/98

(date)

ABSTRACT

A Harshaw LiF TLD card holder was optimized for maximum discrimination between different energies of irradiating photons in order to improve the dosimetric response. Since dose is proportional energy deposited, a theoretical model was created to estimate the TLD response by calculating the energy deposition. These results correlated with experimental data from NIST to within 20%. In order to increase the accuracy of the model, energy deposition calculations were made using the MCNP particle transport program. MCNP improved the correlation of the modeled data with the experimental data. Next, Harshaw's 8825 card holder was optimized for photon energy determination by analyzing the card holder's response with different filter materials and thicknesses. This analysis showed that increasing the copper filter thickness by 20 times and doubling the tin filter thickness compared to the original 8825 design improved the TLD's photon energy determination response. The improved 8825 card holder was constructed and experiments were conducted at Armstrong Laboratories. The MCNP model predicted the experimental response of the card holder to within two standard deviations for all beams except M60. Finally, recommendations for a new card holder were made Naval Dosimetry Center which included a modified filter for improved dose determination.

Keywords: Thermoluminescent Dosimeter, Monte Carlo,
Radiation Transport

ACKNOWLEDGEMENTS

There are many individuals without whom this project would not have been possible. First, the Naval Dosimetry Center (NDC) was instrumental in providing the resources, both physical and technical, used in this project. CAPT Mendenhall, Commanding officer of the NDC, was very supportive during the internship at the NDC during the summer of 1997 and throughout the project. Armstrong Laboratories provided the apparatus and facilities that were used in the experimental portion of the project. Mr. Bruce Dicey, Chief of the Radiation Dosimetry Branch, and MSGT Jocelyn Nixon, Superintendent of the Instrumentation and Calibration Facility, were extremely helpful in this matter. Next, the support of the Naval Academy's Computer Aided Design/ Interactive Graphics (CADIG) staff made the computer modeling possible. Both Doug Richardson and Linda Adlum spent many hours working with the hardware and software to give this project the computer power that made the extensive analyses possible. Finally, Mr. Mike Gibbons provided his technical expertise in the dosimeter construction.

Harshaw Bicron Corporation designed and constructed the 8802 and 8825 card holders as well as the readers used by the NDC. Los Alamos National Laboratories (LANL) developed the MCNP program and it is distributed by the Radiation Safety Information Computation Center (RSICC).

Special thanks go to Prof. Martin E. Nelson, the project advisor, and LT James Cassata, the NDC Science Advisor. The mentorship and guidance these individuals provided was essential. They were always enthusiastic and willing to help, and I will never forget the lessons I learned from them.

TABLE OF CONTENTS

List of Tables	7
List of Figures	8
List of Abbreviations and Symbols	10
Chapter 1: Introduction	13
1.1 Background	13
1.2 Basis for Research	21
Chapter 2: Theoretical Model of a Dosimeter	24
2.1 Theoretical Calculation of Energy Deposition in LiF	24
2.2 Experimental Data and Dose Calculation	30
2.3 Comparison of Experimental Data with Calculations	31
Chapter 3: Monte Carlo Model of a Dosimeter	36
3.1 Monte Carlo Techniques	36
3.2 MCNP-4B	38
3.3 The MCNP Model	40
3.4 MCNP Error Analysis	45
Chapter 4: Correlation of the MCNP Model and Experiment	48
4.1 MCNP Modeling	48
4.2 Comparison of the MCNP Model and Experiment	54
Chapter 5: Optimization of the Card Holder Filter System	58
5.1 The Energy Correction Factor	58
5.2 Analysis of the 8825 Energy Response	60
5.3 Filter Analysis	62
5.4 Conclusions on Filter Optimization	67
Chapter 6: Improved Card Holder Construction	69
6.1 Design and Construction	69
6.2 8825 and 8825I Card Holder Properties	71
Chapter 7: Experimental Verification of Filter Optimization	72
7.1 Experimentation	72
7.2 Data Analysis	76
7.3 Correlation of the MCNP Model and Experiment	78

Chapter 8: Recommendations for a New Card Holder	82
Chapter 9: Conclusions	90
9.1 Conclusions	90
9.2 Recommendations for Further Research	93
Bibliography	94
Appendix A: Card Holder Materials	96
Appendix B: NIST Beam Codes	98
Appendix C: MCNP Input Files	102
C.1 8802 Card Holder MCNP Input File	102
C.2 8825 Card Holder MCNP Input File	105
C.3 8825I Card Holder MCNP Input File	107

LIST OF TABLES

1.1	Quality factors for different types of radiation.	17
2.1	Thermoluminescent chip materials and filter materials for various chip positions in the Harshaw 8802 card holder.	30
4.1	A summary of the changes made to the MCNP model and their effect on error and run time.	54
5.1	Figures of merit for various filter materials and filter thicknesses for the 8825 card holder.	65
5.2	Figures of merit for various filter materials and filter thicknesses for the 8825 card holder with the chip 2 filter correction.	66
6.1	Density thicknesses of the filters in the 8825 and 8825I card holders.	71
7.1	Settings and dose rates for the Seyfert Isovolt X-Ray Generator at the Instrument Calibration Facility.	74
8.1	Summary of current, improved, and proposed card holders.	83
B.1	NIST beam codes and their calibration conditions that are used in this research.	98

LIST OF FIGURES

1.1	Diagram of Harshaw's 8802 card holder.	19
1.2	Diagram of Harshaw's 8825 card holder.	20
1.3	Diagram of Harshaw's 8801 card.	21
2.1	A model of the theoretical photon transport problem.	26
2.2	$R_{n/1}/ODDE_{n/1}$ for various NIST beam codes using theoretical data.	33
2.3	R_2/R_1 and $ODDE_2/ODDE_1$ versus average photon energy of the various beam codes.	35
3.1	Experimental and modeled setup for x-ray irradiations.	42
3.2	Experimental and modeled setup for gamma irradiations.	43
3.3	Experimental and MCNP modeled TLD positions.	44
4.1	Relative number of photons scattered by the phantom that interact with the TLD from different radii from the phantom center.	49
4.2	$R_{n/1}/ODDE_{n/1}$ for various NIST beam codes using MCNP data with electron transport.	55
4.3	$R_{n/1}/ODDE_{n/1}$ for various NIST beam codes using MCNP data without electron transport.	56
4.4	Response ratio of chip 2 to 1 versus average photon energy for the 8802 card holder.	57
5.1	MCNP modeled response ratio R_1/R_2 versus average photon energy for the 8825 card holder	59
5.2	Six possible response ratios for the 8825 card holder.	61
5.3	A typical response ratio and the ideal response ratio versus average photon energy.	64
5.4	Response ratios R_2/R_1 and R_2/R_4 for the 8825 and optimized 8825 card holders versus average photon energy.	67

6.1	Differences in plastic filter thicknesses for the 8825 and 8825I card holders.	70
7.1	Experimental TLD configuration at the Instrument Calibration Facility using four card holders.	73
7.2	Experimental TLD configuration at the Instrument Calibration Facility using one card holder.	75
7.3	The TLD total dose over all irradiations at each phantom position.	77
7.4	Comparison of the response ratios of the experimental data to the modeled data for the 8825 card holder.	79
7.5	Comparison of the response ratios of the experimental data to the modeled data for the 8825I card holder.	80
8.1	Correction factor $C(H_d)$ versus average photon energy for chip 1 of the 8825P card holder.	84
8.2	Modeled average photon energy as a function of the response ratio of chip 2 to 1 for the 8825P card holder.	86
8.3	Modeled average photon energy as a function of the response ratio of chip 2 to 4 for the 8825P card holder.	87
8.4	Modeled average photon energy as a function of the response ratio of chip 3 to 4 for the 8825P card holder.	88
B.1	Relative number of photons versus photon energy for the NIST heavily filtered (H) beams.	99
B.2	Relative number of photons versus photon energy for the NIST medium filtered (M) beams.	100
B.3	Relative number of photons versus photon energy for the NIST lightly filtered (L) beams.	101

LIST OF ABBREVIATIONS AND SYMBOLS

$\gamma(E)$	A photon of energy E
μ	Photon attenuation coefficient (cm^{-1})
μ_{en}	Photon energy absorption coefficient (cm^{-1})
μ_{F}	Photon attenuation coefficient of a metal filter (cm^{-1})
μ_{Li}	Photon attenuation coefficient of LiF (cm^{-1})
σ	Photon microscopic cross-section (b)
ϕ	Photon fluence rate (photons/ cm^2 s)
ϕ_0	Initial photon fluence rate (photons/ cm^2 s)
ϕ_1	Photon fluence rate after the photons have passed through the metal filter (photons/ cm^2 s)
ϕ_2	Photon fluence rate after the photons have passed through the metal filter and LiF (photons/ cm^2 s)
$\phi(x)$	Photon fluence rate as a function of distance inside the LiF chip (photons/ cm^2 s)
a	Metal filter thickness (cm)
A	Area (cm^2)
ABS	Acrylonitrile Butadiene Styrene, a plastic material
b	LiF chip thickness (cm)
$C(H_d)$	Deep dose equivalent correction factor
CADIG	Computer Aided Design/Interactive Graphics
CDDE	Calculated deep dose equivalent (mrem)
D	Absorbed dose (rad)
E	Energy (KeV)
E_m	Average Photon Energy of the m^{th} point on a typical response curve

ECC	Element correction coefficient
ECC _n	Element correction coefficient for chip n
EDDE	Expected deep dose equivalent (mrem)
fom	Figure of Merit
H	Absorbed dose equivalent (mrem)
LANL	Los Alamos National Laboratories
LO	Light output (nC)
LO _n	Light output of chip n (nC)
MCNP	Monte Carlo N Particle transport program
MCNP-4B	Monte Carlo N Particle transport program version 4B
MCP	Magnesium Copper Phosphorus (Copper doped)
N	Number of particles modeled by MCNP
NDC	Naval Dosimetry Center
NIST	National Institute of Standards and Testing
NVLAP	National Voluntary Laboratory Accreditation Program
ODDE	Observed ¹³⁷ Cs equivalent deep dose equivalent
ODDE _n	The ODDE for chip n
ODDE _{n/1}	The ODDE for chip n divided by the ODDE for chip 1
PMMA	Polymethyl methacrylate, a plastic material
PTFE	polytetrafluoroethylene, a plastic material
Q	Quality factor
RCF	Reader calibration factor (nC/mrem)
r	MCNP relative error output

\bar{R}	The output of the MCNP energy deposition tally (MeV)
R_k	Energy deposited by the k^{th} source particle (MeV)
R_n	The energy deposited in or the response of chip n
$R_{i/j}$	The response of chip i divided by the response of chip j
RSICC	Radiation Safety Information Computation Center
S	MCNP estimate of standard deviation
t	Time (s)
TL	Thermoluminescent
TLD	Thermoluminescent Dosimeter
W	Energy deposited (KeV)
x	Distance (cm)

Chapter 1: Introduction

1.1 Background

Accurately measuring the amount of harmful radiation a person receives has been the focus of much research in recent years. Personnel radiation dosimetry is the method by which the amount of radiation, or absorbed dose, is measured and recorded. There are numerous areas where it is important to know the dose a person receives. These areas include nuclear reactor operation, radiation research, and radiation health.

In all these cases, there are health and legal reasons for keeping records of the worker's dose. As ionizing radiation travels through the body, it deposits energy and creates free radicals in the cells. These processes can cause serious biological effects depending on the energy and type of radiation. The effects can therefore be estimated and quantified by knowing the absorbed dose equivalent (H). Furthermore, the absorbed dose is an important factor in radiation medical therapy. Also, state-of-the-art dosimetry is used to establish preventative limits for radiation exposure. Many of these limits are set by federal and state governments and can be used for legal redress by exposed radiation workers.

Dosimetry had a very simple beginning. Initially, a piece of dental film with a paper-clip attached was used to

measure the dose. In this system, significant exposure to radiation caused a detectable shadow to form under the paper-clip on the film. The unit of exposure was then called the paper-clip unit.¹ One paper-clip unit was considered to be a "safe" exposure for one day. At the time this method was used, the biological significance of this and higher doses was unknown. Today there are many types of devices, called dosimeters, which accurately measure the amount of radiation a person receives. Some of these types are the pocket dosimeter, the bubble dosimeter, film badges, and track-etch detectors. Organizations which use these devices are certified through the National Voluntary Laboratory Accreditation Program (NVLAP). They ensure that any organization which operates a dosimetry system meets certain criteria of accuracy in their system.

One organization which operates an extensive dosimetry program is the United States Navy. The Navy operates particle accelerators, radiation health medical facilities, and nuclear reactors on shore and at sea. The Naval Dosimetry Center (NDC) in Bethesda, Maryland oversees the dosimetric needs of the Navy. They are in charge of the Navy's DT648 Whole Body Dosimetry System which includes the dosimeters, the calibration machines, and the readers. The

¹Herman Cember, Introduction To Health Physics (New York: McGraw, 1996) 169.

NDC is able to read and record 30,000 dosimeters per month from shore bases and vessels all over the world. An enormous data base of dosimetric records are kept by the NDC for health and legal reasons. The Navy has regulations about the amount of radiation a worker can receive quarterly and yearly. These are found in the Radiological Affairs Support Program Manual or Rad-10.² The NDC is a NVLAP accredited agency to work with the DT648 Whole Body Dosimetry System.

Thermoluminescent dosimeters (TLD's) are used in the DT648 System. Thermoluminescence is a process where a material emits light when heated. This emitted light is proportional to the radiation received through the following processes. First, ionizing radiation is transported through the thermoluminescent (TL) material. It deposits energy in the material causing electrons to become trapped in an excited state in a dopant. The dopant is usually spread throughout the TL material homogeneously on the order of parts per million. The electrons stay trapped in the excited state for an extended period of time subject to a process called fade where the electrons spontaneously decays to a lower energy state. The fade effect is small over a period of a few months and can be corrected for if the

²United States, Naval Sea Systems Command, Radiological Affairs Support Program Manual, NAVSEA S0420-AA-RAD-010 (1991) II-2.

fading period is known. Next, the TL material is heated by a hot gas, typically nitrogen. The heated material emits light by releasing the electrons from the excited state of the dopant. The amount of light emitted can then be quantified with a photomultiplier tube and other ancillary electronics. Finally, an algorithm is applied to the light output to convert light output to an absorbed dose equivalent. This algorithm takes into account the type and energy of the radiation to develop a correction coefficient which is then multiplied by the light output.

The algorithm is a very important step in the light output to dose conversion because the TL material is not photon tissue equivalent. Photon tissue equivalent materials have the same dose response characteristics as a function of energy as human tissue. If the TL material was tissue equivalent, then no correction factor would have to be applied. For modeling purposes, the approximate composition of tissue is taken to be 10% Hydrogen, 14.9% Carbon, 3.5% Nitrogen, and 71.6% Oxygen by weight.³ The absorbed dose (D) in a material is defined as the energy absorbed per unit mass.⁴ The unit of absorbed dose is the rad (radiation absorbed dose). From the absorbed dose,

³ICRU Report 26. "Neutron Dosimetry for Biology and Medicine" 91.

⁴Cember 189.

another quantity can be defined, the absorbed dose equivalent (H) in units of rems. Because different types of radiation have been found to have different biological effects for the same exposure, the quality factor (Q) is defined with units of rems/rad. The quality factor has different values for different types of radiation as seen in Table 1.1.

Table 1.1 Quality factors for different types of radiation.*

Type of Radiation	Quality Factor (Q)
X-ray	1
Beta	1
Gamma	1
Thermal Neutrons	2
Alpha particles	20

*Cember 278.

The absorbed dose equivalent is then found by using equation (1.1).

$$H = D * Q \quad (1.1)$$

Various types of thermoluminescent materials and dopants are used in today's dosimeters. Some of these are $\text{CaF}_2\text{:Mn}$, $\text{CaSO}_4\text{:Tm}$, $\text{Li}_2\text{B}_4\text{O}_7\text{:Cu}$, and LiF:Mg,Ti . In each of these cases the TL material is followed by the dopant. Also, these materials may have different constituent isotopes which give them various properties. LiF chips containing predominantly ^6Li (TLD-600), ^7Li (TLD-700), or a naturally occurring mixture of the two (TLD-100) are all used because of their different properties in thermal neutron interactions. The Navy is currently using the

LiF:Mg,Ti (magnesium doped) material, but is planning to move to LiF:Mg,Cu,P also known as MCP or copper doped. Both these materials are made by the Harshaw-Bicron Company. The new, copper doped material has been shown to have ten times greater sensitivity for photons and 3.5 times greater sensitivity for neutrons.⁵ The copper doped phosphor also has a fifteen percent decrease in energy dependence below the magnesium doped phosphor which makes it more tissue equivalent.⁶ Also, the fade characteristics of the copper doped material are much less significant than in the magnesium doped TL material.

Along with changing the TL materials, the NDC is also moving to change the holder in which the TLD chips are placed. The current holder is Harshaw's 8802 card holder, shown in Figure 1.1.

⁵James R. Cassata, Improved Personnel Dosimetry Using Copper Doped Lithium Fluoride Thermoluminescent Dosimeters and Neural Network Algorithms, diss., U. of Maryland, 1997, (Ann Arbor: UMI, 1997) 351.

⁶Cassata, Improved 353.

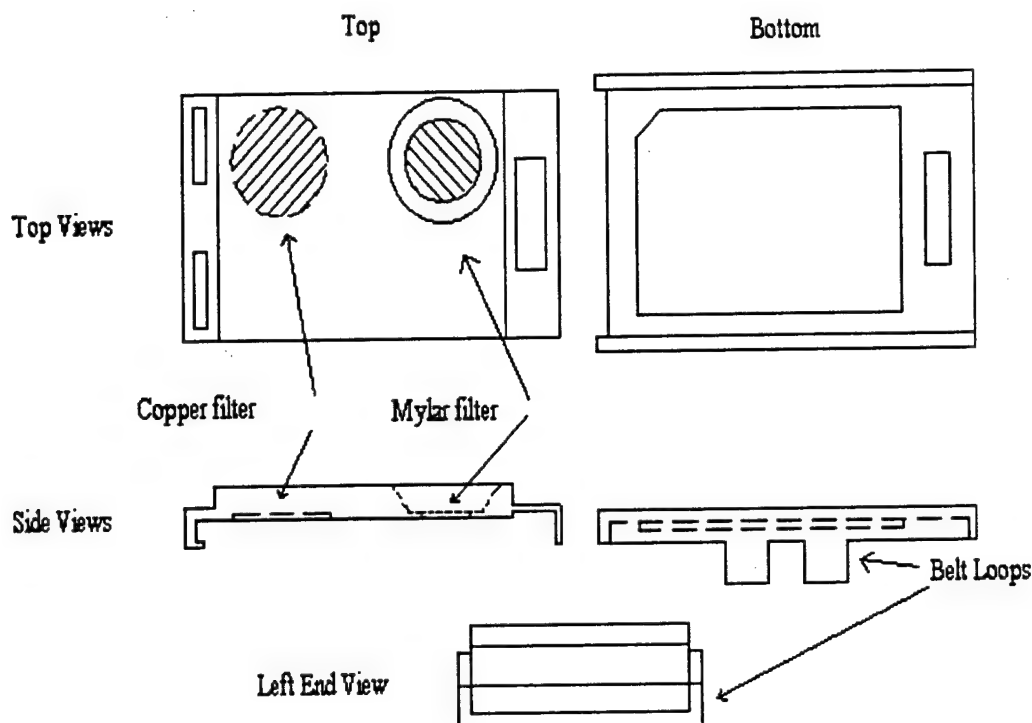


Fig. 1.1 Diagram of Harshaw's 8802 card holder. It is the card holder currently used by the Naval Dosimetry Center.

This holder is made of ABS plastic; it contains two plastic filters, a copper filter, and a Mylar filter. The filter materials are used to shield the TLD chips from varying amounts of x-ray, gamma, and beta radiation. They shield very little neutron radiation because these dosimeters are albedo devices. Albedo devices rely on the human body to scatter thermal neutrons back into the dosimeter where they can then be detected. The proposed card holder is Harshaw's 8825 card holder, shown in Figure 1.2.

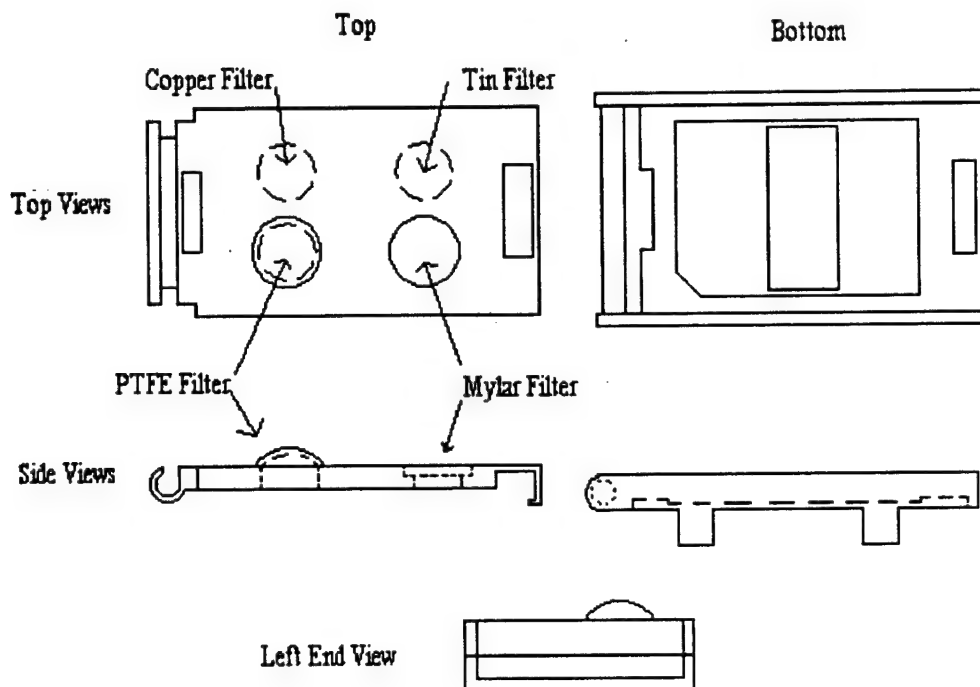


Fig. 1.2 Diagram of Harshaw's 8825 card holder. The Naval Dosimetry Center will be using this card holder in the near future.

This holder is also made of ABS plastic with PTFE, tin, copper, and Mylar filters. ABS, PTFE, and Mylar are all different types of plastics. Because the new holder has a wider variety of filters, it should provide more information about the incident radiation.

The other part of the TLD is the card itself. Figure 1.3 is a drawing of the 8801 Card. It has four different LiF chips encased in polyethelene and held together by an aluminum frame.

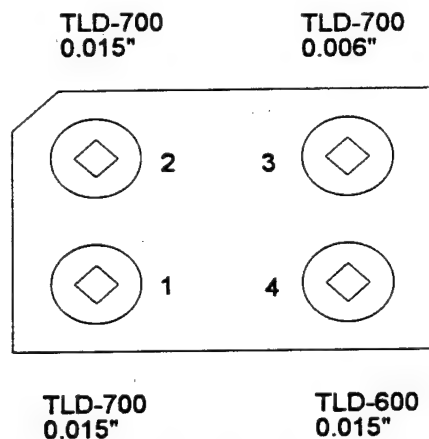


Fig. 1.3 Diagram of Harshaw's 8801 card. It contains four LiF copper doped chips. The composition and thickness of each chip is shown along with its identifying number. This card can be used with either the 8802 or 8825 card holders.

The 8801 Card can be used with either the 8802 or 8825 card holders. The card is inserted into the card holders for the period of exposure, and then the cards are removed from the holders and are sent to be read. Each card also has a bar code identifier to automate the reading process.

1.2 Basis For Research

The purpose of this research is to design an improved TLD so a more accurate absorbed dose measurement can be obtained. There are many reasons why this is necessary. First, the NVLAP standards by which organizations are accredited are becoming increasingly more strict. These organizations are required to send dosimeters to NVLAP where they are irradiated. The dosimeters are then sent back to the organization for reading, and a dose measurement is reported to NVLAP. The accuracy of these reports determines

the accreditation of the organization. Currently, dosimeters must be designed to be accurately read for doses from a few x-ray beams.⁷ Soon the number of possible beams will be increased to 73, encompassing a wider and more complete spectrum of photon energies. NVLAP will also be decreasing the allowed error in reading the dose. The second reason is to obtain more accurate measurement for the health and legal reasons mentioned before. Recent research in the area of dosimetry has concentrated on improving the TL material's characteristics and on the method of heating and reading the dosimeters.⁸ Little optimization of the card holders has been done thus far. The goal of this research is to obtain a set of filter materials and thicknesses which allow better photon energy discrimination so a more accurate correction factor can be applied to the light output, and therefore, a more accurate dose equivalent can be assigned to the user.

The remainder of the paper will be presented in the following manner. Chapter 2 will cover theoretical calculations of dosimetric quantities. Chapter 3 explains Monte Carlo theory and the Monte Carlo model. Chapter 4 involves correlation of the Monte Carlo model results with

⁷James R. Cassata, et al, "Impact of the Revised ANSI Standard on Accredited Thermoluminescent Dosimeter Processors," Radiation Protection Dosimetry 67 (1996): 167.

⁸Y.S. Horowitz, "LiF:Mg,Ti Versus LiF:Mg,Cu,P: The Competition Heats Up," Radiation Protection Dosimetry 47 (1993): 135.

the experimental data. Chapter 5 will cover optimization of the proposed card holder for photon energy discrimination. Chapter 6 deals with constructing the optimized card holder. Chapter 7 presents the experimental results of irradiations with the improved card holder and compares the experimental data with the model predictions. Chapter 8 presents recommendations for a new card holder. Finally, Chapter 9 will discuss the conclusions and recommendations for further research.

Chapter 2: Theoretical Model of a Dosimeter

2.1 Theoretical Calculation of Energy Deposition in LiF

Because the light output of the dosimeter is directly proportional to the energy deposited in the LiF chips,⁹ a theoretical calculation of energy deposition should give results which agree with experiment. Theoretical calculations can also be used to give insight into general irradiation trends and therefore aid in the optimization process.

First, a few radiation transport concepts need to be defined. The photon microscopic cross-section (σ) is a measure of the probability that a photon will interact with an atom. Cross-sections are expressed in barns (b) ($1b = 10^{-24} \text{ cm}^2$). Each element has different cross-sections that vary with photon energy and with the type of interaction involved. The primary interactions present in this experiment are Compton scattering and the photoelectric effect. Compton scattering involves an elastic collision between a photon and a free electron. The photoelectric effect occurs when the photon's energy is transferred to the electron, the photon disappears, and a free electron is emitted from the atom. Another property of the material is its photon attenuation coefficient (μ), which has units of cm^{-1} . The photon attenuation coefficient is equal to the

⁹Cember 369.

microscopic cross-section times the atom density of the material. The total photon attenuation coefficient is the sum of the Compton scattering and the photoelectric attenuation coefficients if the photon energy is less than one MeV. All photons in this project will have energies less than this limit. The photon attenuation coefficient also gives the fraction of the energy in a beam that is removed by the absorber per unit distance.¹⁰ Therefore, if the energy of the Compton scattered photon is excluded, the remaining energy from the interactions is absorbed by the material. This quantity is represented by the photon energy absorption coefficient (μ_{en}). Finally, the photon fluence rate (ϕ) is equal to the number of particles incident on differential area per unit time.¹¹ Fluence rate normally has units of photons/cm² sec.

The following assumptions underlie the theoretical calculations.

- (1) Irradiation by monoenergetic photons with an energy equal to the average energy of the beam's energy spectrum;
- (2) Monodirectional radiation transport;
- (3) Negligible build-up effects in the LiF chips and filters;

¹⁰Cember 147.

¹¹ICRU Report 33, "Radiation Quantities and Units," 7.

- (4) Exponential attenuation of the photon fluence rate in the filter and the chip;
- (5) Pure LiF chips without any dopant because the dopant in the LiF chips is in parts per million;
- (6) ^6Li and ^7Li have the same photon microscopic cross-sections;
- (7) Homogeneous mixture of the constituent elements in ^6LiF and ^7LiF with each having a different photon attenuation coefficient due to the different atom fractions of ^6Li and ^7Li in the LiF.

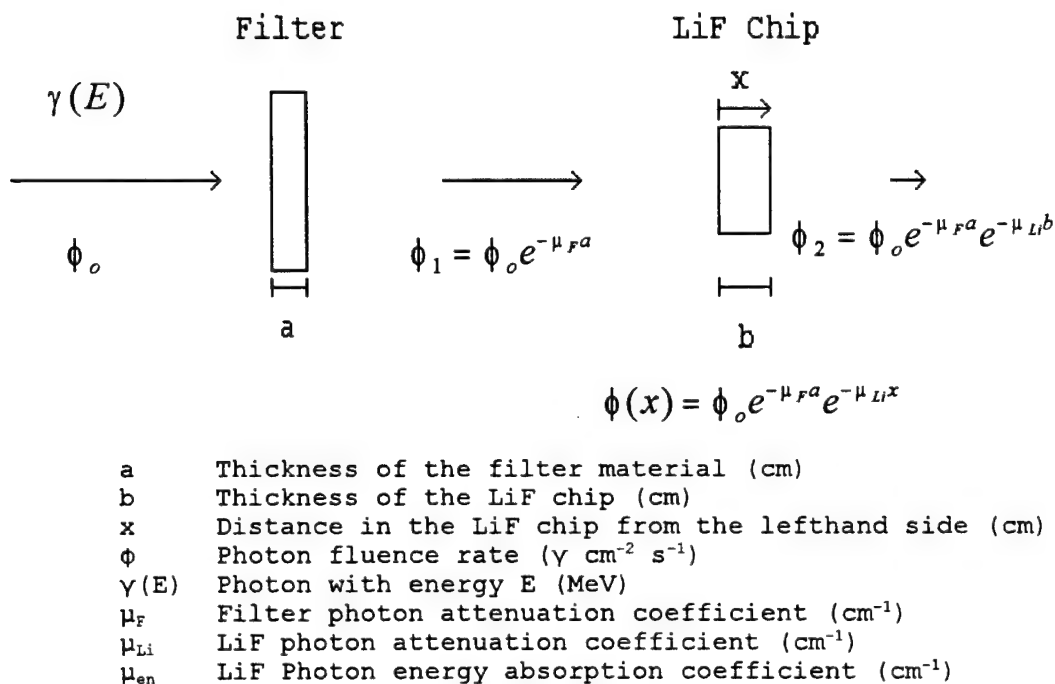


Fig. 2.1 A model of the theoretical photon transport problem. It shows a photon beam of fluence rate ϕ_o and energy E incident on a filter of thickness a and on a LiF chip of thickness b . The photon fluence rate decreases exponentially in the materials. The theoretical model will calculate the energy deposited in the LiF chip.

Figure 2.1 gives a graphical representation of the theoretical problem. A fluence rate and intensity of a photon beam are first decreased by a filter and then the beam deposits its energy in a LiF chip, while simultaneously exponentially decreasing in the chip. The goal is to calculate the theoretical energy deposition from these parameters. There are two different approaches to calculating the theoretical energy deposition, both of which yield the same final equation. First, the differential energy (dW) deposited is equal to the product of the energy of the incident beam (E), the fluence rate in the chip ($\phi(x)$), the probability per unit distance that the photon's energy will be absorbed (μ_{en}), the area of the beam which falls on the the chip (dA), the duration of irradiation (dt), and the differential distance over which the energy is deposited. This relationship is represented by equation (2.1a):

$$dW = E \phi(x) \mu_{en} dA dt dx \quad (2.1a)$$

Inserting the expression for $\phi(x)$ from Figure 2.1 into equation (2.1a) gives equation (2.1b),

$$dW = E \phi_o e^{-\mu_r x} e^{-\mu_{Lx}} \mu_{en} dA dt dx \quad (2.1b)$$

Therefore, the total energy deposited per incident photon is the integral of the right hand side of equation (2.1b) over

the thickness of the LiF chip divided by the number of incident photons ($\phi_o dA dt$). This quantity is expressed in equation (2.2).

$$W/\phi_o dA dt = \int_0^b E e^{-\mu_F a} e^{-\mu_L x} \mu_{en} dx \quad (2.2)$$

$$= E e^{-\mu_F a} \mu_{en} \int_0^b e^{-\mu_L x} dx \quad (2.2a)$$

$$= \frac{E e^{-\mu_F a} \mu_{en} (e^{-\mu_L b} - 1)}{-\mu_L} \quad (2.2b)$$

$$= E e^{-\mu_F a} \frac{\mu_{en}}{\mu_L} (1 - e^{-\mu_L b}) \quad (2.3)$$

Equation (2.3) gives the final expression for energy deposited per incident photon in a chip of thickness b filtered by a metal of thickness a .

The second approach is to make use of the principle of energy conservation. The energy deposited (W) is equal to the product of the energy of a photon, the difference in fluence rates entering and exiting a material ($\phi_1 - \phi_2$), the area of the beam (dA), and the duration of the irradiation (dt).

$$W = E(\phi_1 - \phi_2) dA dt \quad (2.4)$$

Using the expressions for ϕ_1 and ϕ_2 as shown in figure 2.1, equation (2.4) can be expanded to equation (2.4a).

$$W = E(\phi_o e^{-\mu_F a} - \phi_o e^{-\mu_F a} e^{-\mu_L b}) dA dt \quad (2.4a)$$

This expression assumes that every photon that interacts in the chip material deposits its energy. This is an incorrect assumption due to the Compton scattering effect. Therefore, μ_{en}/μ_{Li} becomes the fraction of attenuated photons that deposit their energy in the material. Multiplying by this factor and dividing through by the number of incident photons ($\phi_0 dA dt$) gives equation (2.4b).

$$\frac{W}{\phi_0 dA dt} = E e^{-\mu_F a} \frac{\mu_{en}}{\mu_{Li}} (1 - e^{-\mu_{Li} b}) \quad (2.4b)$$

Equation (2.4b) agrees with equation (2.3), showing that the two approaches are equivalent.

If the material where the energy is deposited is very thin, one may assume that $e^{-\mu_{Li} x} \approx 1 - \mu_{Li} x$. Applying this approximation to equation (2.4b) gives equation (2.5).

$$\frac{W}{\phi_0} e^{-\mu_F a} dA dt \approx E \mu_{en} b \quad (2.5)$$

Equation (2.5) agrees with the definition of the photon energy absorption coefficient found in Shapiro.¹²

These calculations can be made for each chip and filter combination in the dosimeter. The final calculation of energy deposition for a chip in position n is given the

¹²Jacob Shapiro, Radiation Protection (Cambridge:Harvard Press, 1981) 37.

symbol R_n for the response of chip n , where n can vary from 1 to 4. The filters and chip numbers for the current, 8802, card holder are given in Table 2.1.

Table 2.1 Thermoluminescent chip materials and filter materials for various chip positions in the Harshaw 8802 Card Holder.

Chip Position	Chip Material	Filter Material
1	TLD-700	ABS plastic
2	TLD-700	ABS plastic and Copper
3	TLD-700	Mylar
4	TLD-600	ABS plastic

A complete description of the card holder materials is given in Appendix A.

2.2 Experimental Data and Dose Calculations

The experimental data for the initial stages of this project were supplied by the Naval Dosimetry Center (NDC). This data represents a few thousand irradiations of the copper doped LiF chips in the 8802 Card Holder. The irradiations were done at the National Institute of Standards and Testing (NIST), and the cards were read at the NDC. Reading the cards consisted of heating the LiF chips and measuring their light output (LO) with a photomultiplier tube. The charge on the photomultiplier tube was measured in nanocoulombs. The ^{137}Cs equivalent deep dose equivalent dose received by the chip was then calculated by use of

equation (2.6).¹³

$$ODDE_n = LO_n ECC_n / RCF \quad (2.6)$$

The light output (LO_n) is the measured value of light emitted by chip n in units of nanocoulombs (nC). The element correction coefficient (ECC_n) is a dimensionless quantity which corrects the light output of an individual chip n to a reference sensitivity.¹⁴ This factor is needed because different chips may respond differently to the same radiation source due to small differences in size, shape, mass, and composition. The reader calibration factor (RCF) converts the light output to an observed ^{137}Cs equivalent deep dose equivalent for chip n ($ODDE_n$).¹⁵ The RCF has units of nC/mrem.

The experimental data consisted of dose measurements for the four LiF chips irradiated with five different x-ray and gamma energy spectra. For each energy spectrum, there were three different exposure times, each with 15 separate trials which were all averaged to obtain a dose measurement for each of four chips. The x-ray and gamma energy spectra are explained in Chapter 3.

¹³Cassata Improved 91.

¹⁴Cassata Improved xxiv.

¹⁵Cassata Improved xxiv.

2.3 Comparison of Experimental Data with Calculations

In order to compare the theoretical measurements with the experimental data, the doses of the different chips were normalized to chip 1. In other words, four ratios were compared; each R_n/R_1 was compared to each $ODDE_n/ODDE_1$ where n varied from one to four. Another way of expressing their ratios are $R(n/1)$, $R_{n/1}$, $ODDE(n/1)$, and $ODDE_{n/1}$. Since energy deposited and ODDE are proportional to light output, the calculated energy deposited should be proportional to the ODDE. Equation (2.7) defines this relationship.

$$\left(\frac{R_n}{R_1}\right) = \left(\frac{ODDE_n}{ODDE_1}\right) \quad (2.7)$$

In equation (2.7), R_n has units of MeV and $ODDE_n$ has units of mrem. If each R_n is normalized with R_1 and each $ODDE_n$ is normalized with $ODDE_1$ then these two dimensionless ratios should be equal as shown in equation (2.7). Because chip 3 has less mass than chip 1, a correction factor must be applied to $R_{3/1}$ to correct to an $ODDE_{3/1}$. The ratio $ODDE_{3/1}$ has units of mrem/mrem which is a representation of energy per unit mass. Chip 1 is .0015" thick and chip 3 is .0006" thick so the correction factor is 15/6. Figures 2.2a through 2.2d show the comparison between $R_{n/1}$ and $ODDE_{n/1}$ for the five beams studied.

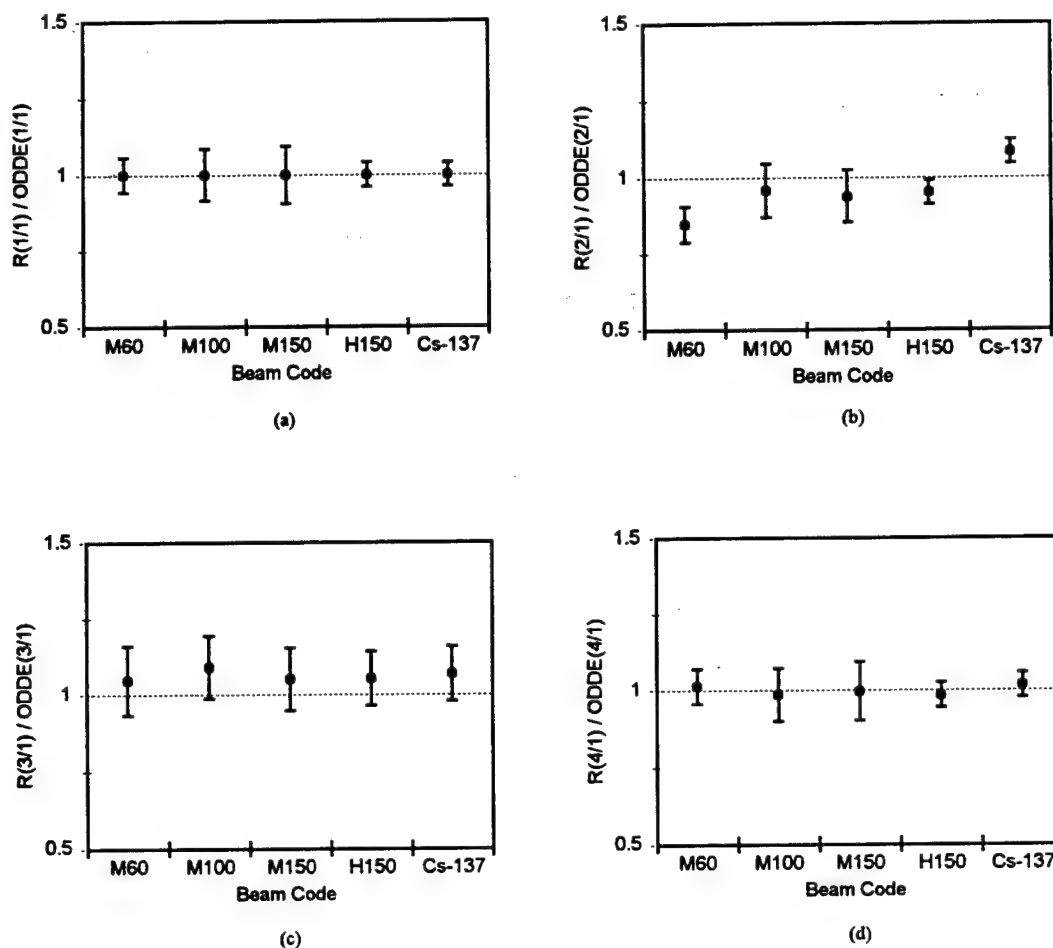


Fig. 2.2 $R_{n/1}/ODDE_{n/1}$ for various NIST beam codes using theoretical data. The error bar represents one standard deviation from the calculated value which falls in the middle of the bar. The expected value of the ratio is one. These graphs show a high correlation between the theoretical model and the experimental data.

Each of these ratios had a relative error of less than 10% except for the 18.2% error in R_2/R_1 for the M60 energy spectrum. The expected value of all chip responses over all the beams fell within one standard deviation of the calculated value 80% of the time and within two standard

deviations 86.7% of the time. These results were reasonable because the standard gaussian probability distribution predicts that 68% of the measurements will be within one standard deviation and 95% within two standard deviations. This data was also a preliminary confirmation that energy deposition is proportional to light output. They also suggested that a more detailed theoretical analysis would lead to a better correlation. A possible explanation for the 18.2% error in the M60 beam is that the energy spectrum over which M60 is distributed contains copper's photoelectric edge energy. The copper photoelectric edge is a discontinuity in the attenuation coefficient versus energy plot which makes copper's attenuation response difficult to model when using only the average energy of the M60 energy spectrum. Finally, figure 2.3 gives the dose response ratio versus average photon energy for the 8802 Card Holder. In this figure the experimental data is given by the ratio $ODDE_2/ODDE_1$ and the predicted data is the ratio R_2/R_1 . As can be seen, a strong correlation is shown between theory and experiment.

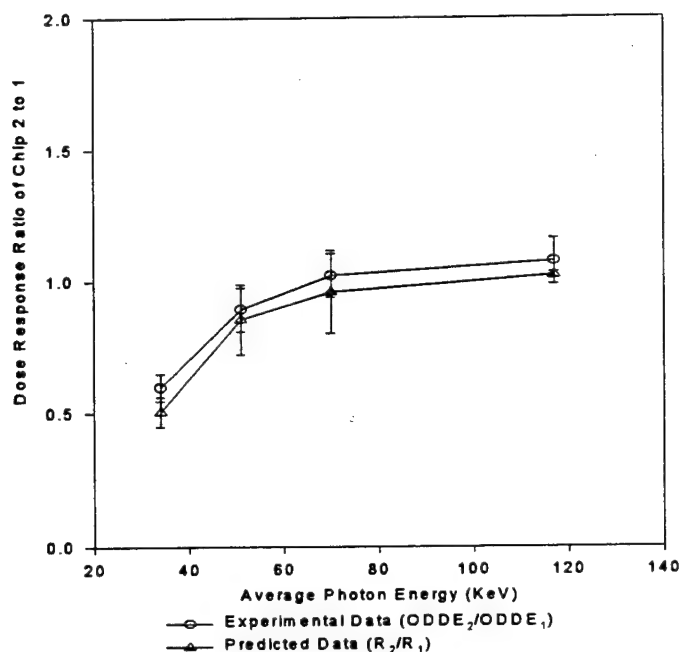


Fig. 2.3 R_2/R_1 and $ODDE_2/ODDE_1$ versus average photon energy of the various beam codes. The error bars show two standard deviations from the correct value. This graph shows the strong correlation between the theory and experiment.

The ratios R_2/R_1 and $ODDE_2/ODDE_1$ vary more with energy than the other ratios. In fact, the $ODDE_2/ODDE_1$ ratio is used to calculate the energy correction factor for the current dosimeter. Figure 2.3 gives another indication of the strong correlation between these theoretical calculations and the experimental data. These results suggested that a computer analysis that made fewer assumptions, especially about the photon spectrum, would be more accurate than these relatively simple theoretical calculations.

Chapter 3: Monte Carlo Model of a Dosimeter

3.1 Monte Carlo Techniques

Monte Carlo methods are numerical techniques which use random sampling of probability distributions to create individual microscopic case histories which are then averaged to estimate the solution to a macroscopic physical problem. In particle transport problems, the simulation starts with a particle source and a modeled physical system. Distributions are sampled randomly to obtain the energy and direction of flight of the source particles. Over a large number of source particle histories, the simulation eventually follows the physical source characteristics. After the particle leaves the source, it can interact and collide with atomic matter in many ways. The probability distributions of these interactions depend primarily on the colliding particle's energy, the type of particle, and the atomic properties of the matter. The "life" of one of these particles is governed by many random processes.¹⁶ First the particle is started from the source. Then, the distance traveled in a medium between interactions, the energy of the scattered particle, its direction of flight, and the number of secondary particles that are created are all governed by

¹⁶Ivan Lux, Monte Carlo Particle Transport Methods (Boston: CRC Press, 1991) 33.

probability distributions.¹⁷ Finally, when the particle's energy drops below a certain threshold or when the particle is absorbed, the simulation begins a new history. Random numbers are generated within distributions at each event to determine the particle's path and energy. Slight differences in this scheme arise when electrons are transported through matter since they are charged particles. Where a neutron might undergo thirty collisions slowing down in matter, a photon will experience fewer than ten, and an electron will undergo on the order of 10^5 individual interactions.¹⁸ This makes single interaction Monte Carlo solutions difficult. A different approach is taken for the electrons. The energy loss and angular deflection of the particle is taken from a probability distribution based on multiple scattering theories so many interactions can be treated at once. This is known as "condensed history" Monte Carlo method.¹⁹

This life of randomly determined interactions is called the particle's random walk. The final solution to the problem involves averaging the particle's behavior over a large number of these particle histories or random walks. As the number of histories increases, the problem solution

¹⁷Lux 33.

¹⁸Grady H. Hughes, "Treating Electron Transport in MCNP," 1.

¹⁹Hughes 1.

approaches the expected value. This does not always mean that the simulation approaches the observed physical situation. There are many questions to be considered here. How well is the probability density function governing the physical processes known? How well are the random numbers sampling the distribution? Does the simulation sufficiently model the physical world before the interactions?²⁰ These are all questions which must be addressed before the physical accuracy of the model can be determined.

3.2 MCNP-4B

The Monte Carlo simulation of interest here is the Monte Carlo N Particle transport code (MCNP). This program was developed at Los Alamos National Laboratory (LANL) and continues to be updated there. The version of MCNP used here is MCNP-4B. The program is distributed by the Radiation Safety Information Computation Center (RISCC). The code is a computer based program that can currently be implemented on a large number of platforms. For this project, MCNP was installed on three different platforms with different capabilities at the U.S. Naval Academy. First, MCNP was loaded onto Superaero, a UNIX system in the Naval Academy's Computer Aided Design/ Interactive Graphics (CADIG) laboratory. This supercomputer provided four

²⁰Lux 33.

processors that had the potential to be used in parallel for different applications. At first, one simulation could be run on each of the four processors simultaneously. It was hoped that by running the four processors in parallel with one simulation at a time, the cumulative effects of the parallel processing would increase the overall simulation speed. This project was unsuccessful at running MCNP with parallel processors on this system. MCNP was then installed on both a 166 MHz and a 233 MHz personal computer. The personal computers had the advantage of speed over the Superaero computer, but they could only run one program where Superaero could run four. Finally, MCNP was loaded on a central server which could be accessed simultaneously by eighteen SUN workstations in CADIG. Superaero was eventually abandoned in favor of the SUN workstations. The 233 MHz personal computer was used for longer, higher energy problems because of its relative speed.

In all cases where MCNP was installed on a new platform, test programs were run which ensured that MCNP was working properly. These test programs came with the code and are an essential part of the installation process. In all cases the test programs showed that there were no errors in the installation or in the execution of the program.

MCNP-4B has various capabilities which were essential to this project. The program is able to model the transport

of neutrons, photons, and electrons. Photons and electrons were the particles of interest in this project, but further analysis may involve neutron modeling. MCNP has libraries of energy dependant cross sectional data for each element. The photon library, MCPLIB02, was expanded from earlier versions of MCNP. The library contains data from the Livermore Evaluated Photon Data Library (EDPL) with an energy range of 1 KeV to 100 GeV. This library was used extensively in this project. These cross sections had to be very accurate to model an actual physical situation properly. Also important was the electron library EL1 which contained information for electron interaction cross sections. Another feature of the MCNP-4B program was its graphical capabilities. These were essential to verifying that the computer model was geometrically correct. The program was also able to display the information for the various cross section libraries as a graph of cross section versus energy.

3.3 The MCNP model

The most important step in the MCNP analysis of the 8802 Card Holder was modeling the physical experimental setup. The initial model contained every relevant part of the experimental apparatus with which the NDC data was taken. In the following chapter, changes to this original

model will be discussed. The underlying theme of this stage of the modeling was to create objects which had the simplest geometrical shapes so that the MCNP program would have little trouble with the transport problems. Surfaces were kept at right angles to each other whenever possible, and only planes, cylinders, and spheres were used to construct the different parts of the apparatus. First, the 8802 Card Holder and the 8801 Card were modeled. The exact dimensions of the card holder were used in all cases with a few simplifying assumptions. Plastic pieces which did not significantly filter photons traveling toward the TLD card were discarded. This included such pieces as the belt loops and the extreme ends of the card holder.

Next, the x-ray and gamma spectra were modeled for a calibrated NIST facility. X-rays are created by accelerating electrons at a tungsten target through an accelerating potential given in units of kV. When the electrons slow down in the target, they release energy in the form of x-rays that have an energy which depends on the material and on the accelerating voltage. The maximum energy a photon can have is given by multiplying the fundamental charge of the electron times the accelerating potential. The x-rays then pass through filters of three different major categories, light (L), medium (M), and heavy (H). The combination of the type of filter and the

accelerating voltage give the beam its identifier. For example, M60 would be a medium filtered beam with a 60 kV accelerating potential. The exact filter varies between beam codes of the same category. For instance M100 uses an aluminum filter while M150 uses an aluminum and copper filter. The various beam codes and their calibration conditions are given in Appendix B. However, neither the tungsten target nor the metal filters were used in the modeling. The spectrum of the photons which have already passed through the filter are tabulated by NIST for each beam code. This data was obtained from NIST in diskette form²¹. The spectrum gave a number of photons or counts at a given energy in units of keV. This data was entered into the model for each beam code of interest. This process was much easier for the gamma irradiations since the gamma beam is nearly monoenergetic from ^{137}Cs at 662 KeV.

Next, the geometrical configuration of the x-ray or gamma beam itself was entered into the model. The basic x-ray experimental configuration is shown in Figure 3.1.

²¹Chris Soares, "Spectral Files" diskette, (National Institute of Standards and Testing).

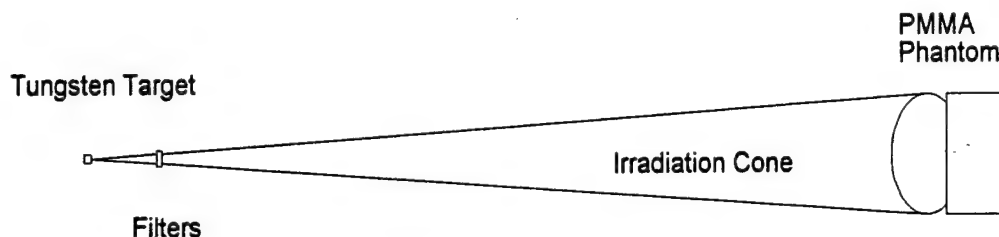


Fig 3.1 Experimental and modeled setup for the x-ray irradiations. For the x-ray beams, the modeled photons were started at the filters instead of the tungsten target. The PMMA phantom was 2 meters from the target, and the TLD's were placed on the front face of the phantom. The irradiation cone has a radius of 15 cm at the phantom.

The photon source was taken to be the metal filter instead of the tungsten target because the energy distribution of the photons was known only after the photons had passed through the filter. The angular data for the size of the irradiation cone, the cone through which the photons propagate, was obtained by considering the dimensions of the tungsten source. The radius of the irradiation cone was 15 cm at the phantom. The irradiation cone extended to the PMMA phantom where the TLD's were irradiated, and air was used as the medium between the source and the phantom.

Similarly, the basic gamma experimental configuration is given by figure 3.2.



Fig. 3.2 Experimental and modeled setup for gamma irradiations. In this setup, the gamma rays began at the ^{137}Cs source and there were no filters. The phantom was placed at 195 cm from the source and the TLD's were placed on the front face of the phantom.

In the gamma model, the actual ^{137}Cs disk source was used as the photon source. There was no filter in this beam. The irradiation cone dimensions changed slightly, but otherwise, this model was similar to that used for the x-rays.

Next the TLD's position was modeled. The TLD was placed on a PMMA plastic block which is called a phantom with a frontal area of 30 cm by 30 cm and a depth of 15 cm. The phantom replaced the human body in TLD experiments. In the experimental data from the NDC, four TLD's were positioned on the phantom for each irradiation as seen in Figure 3.3a. Because the irradiating beam was known to provide a uniform field over the 15 cm radius being modeled and because only chip ratios were being studied, only one centered dosimeter was necessary for the model. This is shown in Figure 3.3b.

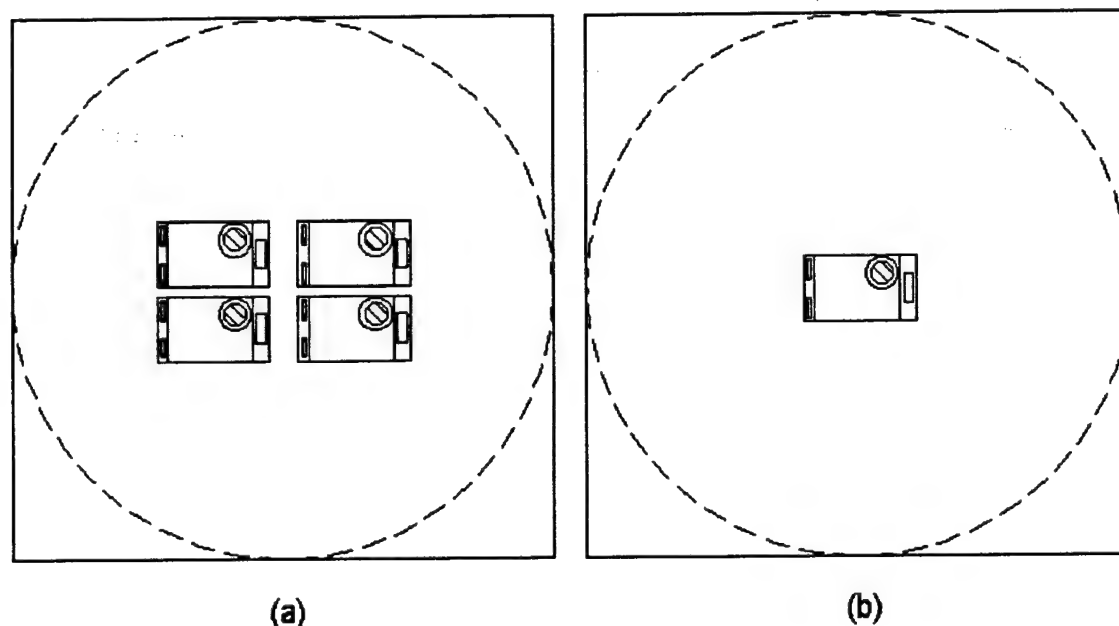


Fig. 3.3 Experimental and MCNP modeled TLD positions. (Fig 3.3a and b) The square box is the phantom and the dotted circle represents the area that is being irradiated.

Finally, MCNP was used to calculate the energy deposition in the LiF chips. This energy deposition tally also followed a randomly sampled probability distribution. At each interaction in the LiF, a photon will deposit a certain amount of energy, and MCNP tallies each small energy deposition to give the total amount of energy deposited in each LiF chip. This was an important model output parameter.

3.4 MCNP Error Analysis

In addition to the energy deposition tally, MCNP gives a relative error based on the statistics of the problem. As stated previously, MCNP approaches the expected solution to

a given problem over a large number of particles. The relative error value given by MCNP varies inversely with the square root of the number of particles histories in the problem. For example, quadrupling the number of particle histories which are modeled, halves the relative error value. There are other methods which decrease the relative error of a tally; they will be discussed in the next chapter.

The MCNP standard deviation is calculated in the following manner: First, let \bar{R} be the output value of the MCNP energy deposition tally, let N be the number of source particles modeled, and let R_k be the energy deposited by the k^{th} source particle. Equation (3.1)²² gives the value for \bar{R} .

$$\bar{R} = \frac{1}{N} \sum_{k=1}^N R_k \quad (3.1)$$

Next, the MCNP estimates the standard deviation (S) using equations (3.2a)²³ and (3.2b).

$$S^2 = \frac{1}{N} \sum_{k=1}^N \frac{(R_k - \bar{R})^2}{N-1} \quad (3.2a)$$

²²Judith Briesmeister, MCNP - A General Monte Carlo N-Particle Transport Code. Version 4B (LA-12625-M, 1997) 2-89.

²³Briesmeister, 2-89.

$$S = \sqrt{S^2} \quad (3.2b)$$

Finally, the MCNP relative error output (r) is calculated by equation (3.3).

$$r = \frac{S}{\bar{R}} \quad (3.3)$$

These equations are important for two reasons. First, they show how the relative error decreases with the number of particle histories. Second, they define the output parameters (\bar{R} , r) for the energy deposition tally which is performed in each LiF chip.

The final input parameter to the MCNP model that needs to be discussed is the random number seed. The random number seed determines the manner in which each distribution will be sampled throughout the problem. All subsequent random numbers are calculated using this seed. Two identical input files with the same random number seed will produce identical output parameters. Varying the random number seed between runs has little effect for problems with a large number of particles since the problem is approaching an expected value. The random number seed was left at the default value for all the MCNP runs except those that investigate the effect of varying the random number seed.

The MCNP input files were created and continually

modified with the principles contained in this chapter.

Input files of the various models created in subsequent chapters are given Appendix C. The next major step was to correlate the MCNP modeling results with the experimental data on the 8802 card holder.. This is described in Chapter 4.

Chapter 4: Correlation of the MCNP Model and Experiment

4.1 MCNP Modeling

The initial MCNP model which was created using the methodology from Chapter 3 did not correlate well with the experimental data and it also had a lengthy run time for a small number of particles. In fact, a 166 MHz computer took 9 hours to model 5 million particles. The goals of this section of the project were to increase the accuracy of the model and to decrease the model run time. Two general themes were employed to accomplish these goals. First, by increasing the number of photon interactions modeled in the chips, the MCNP calculated error was reduced. Second, eliminating unnecessary particles from the model decreased the model run time.

The first change involved directing more particles toward the LiF chips to decrease the MCNP calculated error. This was accomplished by decreasing the radius of the cone through which the photons propagate toward the phantom. Originally, the photons were spread out over a disk of radius 15 cm at the phantom as in the experimental apparatus. A large portion of the photons were falling on the phantom and were not interacting with the TLD's. Decreasing the size of this disk, while keeping the number of particles modeled constant, would in effect cause more particles to be directed toward the TLD, increasing the

probability of a particular photon interacting with the LiF chip.

A major consideration here was the photons which scatter off the phantom and return to the TLD, a process called backscatter. Before the size of the irradiation cone could be decreased, the number of photons which scattered toward the TLD's from various regions of the phantom had to be determined. Figure 4.1 gives the relative number of photons which scattered into the TLD as a function of the radius from the phantom's center.

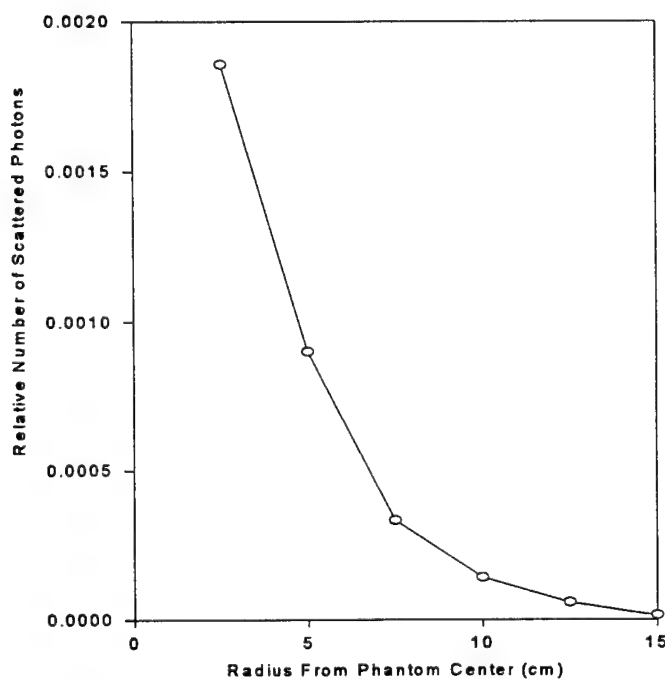


Fig 4.1 Relative number of photons which are scattered by the phantom that interact with the TLD from different radii from the phantom center. Over 90% of the interacting, scattered photons come from inside a radius of 7.5 cm. This analysis was conducted with the MCNP program.

An analysis of the area under the curve in Figure 4.1 indicates that more than 90% of the photons come from a radius of 7.5 cm from the center of the beam. The result of this analysis was that the photon irradiation cone could be reduced to a radius of 7.5 cm at the phantom. Since the area over which the photons were directed had decreased by a fourth, it was expected that the photon interactions in the LiF chip would increase by a factor of four. The observed increase was slightly higher than that.

The next modification to the model involved eliminating unnecessary particle tracks and collisions to decrease the model run time. First the phantom was changed from a box 30 cm by 30 cm on the front face to a cylinder of radius 9 cm to reflect the smaller irradiation cone and the backscatter analysis. Also, the thickness of the phantom was decreased to a thickness of three photon mean free paths. The average mean free path of a photon in the phantom was 3.5 cm for the lowest energy beam where the most scatter is expected. The phantom was therefore decreased from a thickness of 15 cm to 10.5 cm. These two changes combined cut the model run time in half by eliminating photon collisions in the phantom which did not contribute significantly to the energy deposition tallies in the LiF chips.

The next changes to the model were directed at decreasing the MCNP relative error value. Decreasing the

size of the irradiation area had increased the interacting particles by four times and so had already decreased the relative error by half. Further increasing the number of particles interacting in the LiF chips decreased the error further as seen in the next modifications.

The third modification to the model was the MCNP particle weighting technique. The model is composed of many cells bounded by surfaces from the input file. Each cell in the MCNP model has a statistical importance associated with it. In the original model, each cell had a photon importance of one, meaning that each cell treated particles in the same statistical manner. In this modification, the photon importance in the LiF chips was changed from one to three. When a photon moved from a cell of photon importance one to a cell of photon importance three, the one particle was split into three separate particles, each with one third the statistical weight.²⁴ This allowed for more energy deposition collisions to occur within the LiF chip without changing the original statistical nature of the problem. An importance of three was chosen to increase the particle collisions significantly without damaging the statistics of the problem. MCNP warns the user of importances of four or greater due to their uncertain statistical nature. This technique did increase the number of photon interactions in

²⁴Briesmeister, 3-29.

the LiF by a factor of three, and therefore decreased the relative error by a factor of the square root of three.

The final MCNP technique used was the forced collision technique. In this technique, MCNP divides a population of photons into a collided and an uncollided part as a function of the microscopic cross section of the material.²⁵ The uncollided part will not interact with the cell, but the collided part will be forced to undergo collisions with the cell. This technique did increase the collisions within the LiF chips, but it did not decrease the error as much as the importance technique did. For this reason, the forced collision technique was not adopted.

The final modification to the model involved considering electron energy deposition in the LiF chips. After the MCNP model was run with the decreased irradiation cone and the photon particle weight of three in the LiF chips, all relative errors between the model and the experimental data fell below 10% except for the ratio R_2/R_1 . It was also noticed that chip 2 had the highest number of electron interactions taking place within the chip. There were on the order of 30 times more electrons entering chip 2 than any other chip. This was due to the copper filter in place over chip 2. In the model, electrons are being emitted from the copper and are depositing their energy in

²⁵Briesmeister, 2-131.

the LiF chips in a manner that did not correlate with experiment. Two methods were tried to correct this problem. First, electron transport was taken completely out of the model so that only photon transport was modeled. In this case, interactions between the electrons and photons were still modeled but only photons were tracked through the matter. Second, the electron importances were set to zero inside the LiF chips. This approach stopped the electrons from depositing their energy in the chips, but allowed other electron interactions to occur outside the chips.

The model which excluded electron transport correlated the most closely with the experimental data. Additionally, the run time of the model was decreased by a factor of ten, allowing for a greater number of particles to be modeled in the same amount of time. This is a significant finding for future TLD modeling. Since the electron mean free path in the LiF was approximately 100 to 1000 times less than the thickness of the chip, the electrons deposited their energy very near the surface of the LiF chips and so did not significantly interact with the dopant to produce trapped electrons. Thus, the energy deposited by the electrons has very little impact on the measured light output produced by the chip. Therefore, electron transport was excluded from the model.

Table 4.1 gives a summary of the changes made to the

original MCNP model. Each modification to the model is discussed along with its corresponding effect on relative error decrease and the decrease in total run time.

Table 4.1 A summary of the changes made to the MCNP model and their effect on error and run time. (N/A = Not Available)

Modification	Relative Error Decrease	Run Time
1. Decrease the radius of the irradiation cone and decreasing the phantom thickness	1/2	1/2
2. Increase the particle importance within the LiF chips to 3	$1/\sqrt{3}$	no effect
3. Forced collision technique (This modification was not adopted into the model)	N/A	N/A
4. Remove electron transport from the model	Various effects	1/4

4.2 Comparison of the MCNP Model and Experiment

The following figures show the correlation between the MCNP model and the experimental data. The models both with and without electron transport have been included for comparison. Figures 4.2a through 4.2d show the correlation between the MCNP model with electron transport and the experimental data.

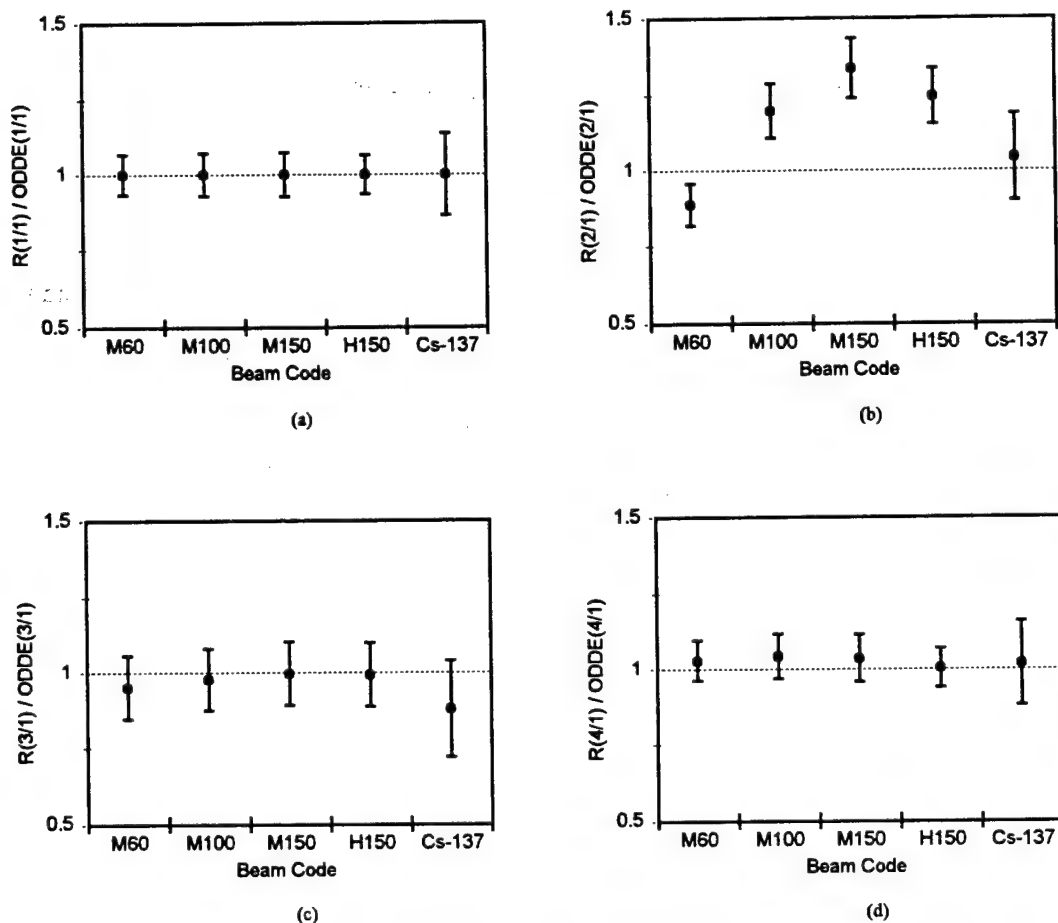
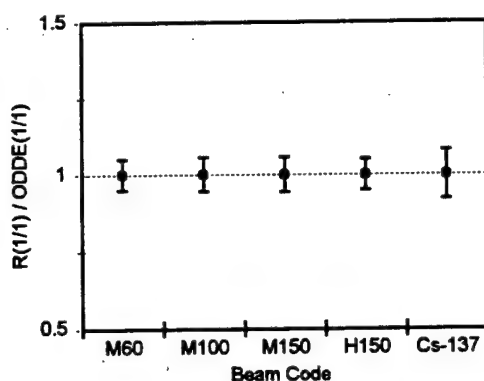
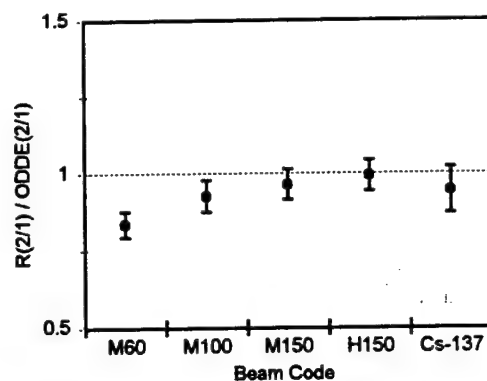


Fig 4.2 $R_{n/1} / ODDE_{n/1}$ for various NIST beam codes using MCNP data with electron transport. The error bar represents one standard deviation from the calculated value which falls in the middle of the error bar. The expected value of the ratio is one. These graphs suggest a poor correlation between an MCNP model which contains photon and electron transport and experiment.

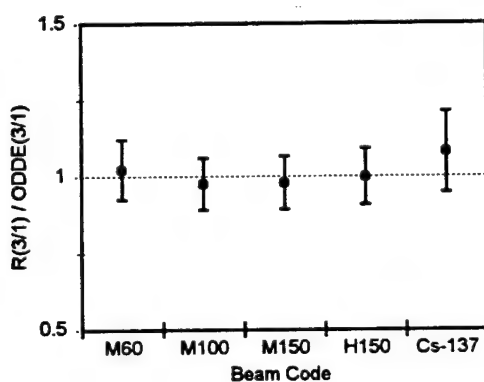
As shown in figure 4.2b, the ratio $R_{2/1} / ODDE_{2/1}$ does not fall within one standard deviation of the expected unity value for the x-ray beams. Figures 4.3a through 4.3c show the model which excludes electron transport.



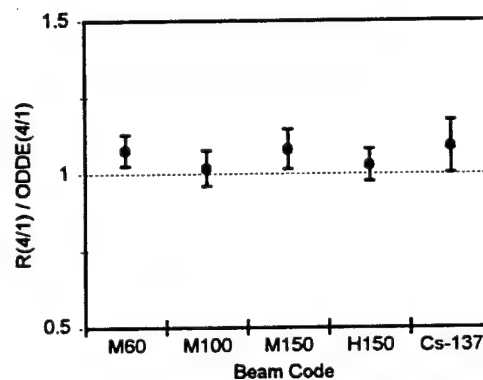
(a)



(b)



(c)



(d)

Fig 4.3 $R_{n/1} / ODDE_{n/1}$ for various NIST beam codes using MCNP data without electron transport. The error bar represents one standard deviation from the calculated value which falls in the middle of the error bar. The expected value of the ratio is one. These graphs show that the model which does not contain electron transport correlates better with experimental data than the model that does.

This model correlates better for all ratios than the model which included electron transport. Finally, figures 4.4a and 4.4b show the comparison of the modeled and experimental ratios of chip 2 to 1 versus photon energy.

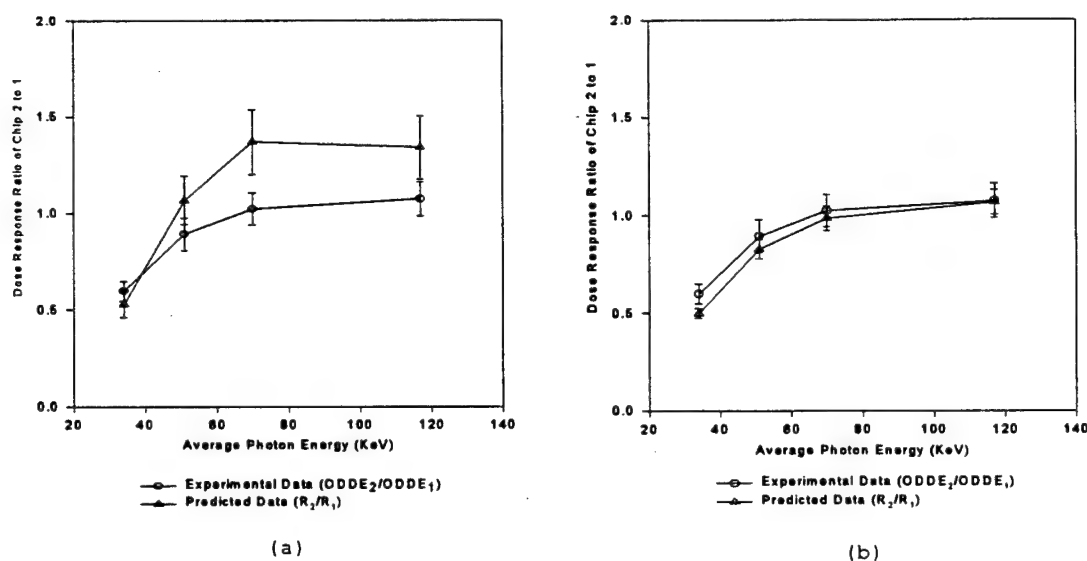


Fig 4.4 Response ratio of chip 2 to 1 versus average photon energy for the 8802 card holder. The error bar represents two standard deviations. Fig 4.4a uses the model which contains both photon and electron transport while Fig 4.4b uses the model which excludes electron transport. The MCNP data which excludes electron transport correlates the most closely with experimental data.

Figure 4.4a uses data from the model which contains both photon and electron transport and figure 4.4b represents the model without electron transport. The model which does not include electron transport clearly correlates better than the model that does. This is a significant result for future modeling of thermoluminescent materials which have a low dopant concentration.

Chapter 5: Optimization of the Card Holder Filter System

5.1 The Energy Correction Factor

The goal of this project is to optimize the 8825 card holder for photon energy discrimination in order to obtain a more accurate energy correction factor and therefore a more accurate dose measurement. The energy correction factor, $C(H_d)$, is determined by an algorithm in the reader and is applied to the observed ^{137}Cs equivalent deep dose equivalent (ODDE). The $C(H_d)$ corrects the ODDE measurement to the calculated deep dose equivalent (CDDE). This is necessary because the LiF chips respond differently to different energies and types of radiation than to the photons emitted by ^{137}Cs .²⁶ This relationship is expressed by equation (5.1).

$$CDDE = C(H_d) \cdot ODDE \quad (5.1)$$

The $C(H_d)$ factor is currently determined experimentally for a particular NIST beam code by dividing the expected deep dose equivalent (EDDE) by the measured (ODDE) as shown in equation (5.2)²⁷

$$C(H_d) = EDDE / ODDE \quad (5.2)$$

This calculation is repeated for 15 irradiations and an

²⁶Cassata, Improved 62.

²⁷Cassata, Improved 62.

average $C(H_d)$ is determined.²⁸ These correction factors and their corresponding energies are then processed by the reading algorithm. The algorithm chooses which $C(H_d)$ to use by looking at chip response ratios. The current Navy 8802 system uses only the ratio of chip 1 to 2 ($ODDE_1/ODDE_2$) to determine which $C(H_d)$ to use.²⁹ This report normally plots the ratio of chip 2 to 1, but in this case, the Navy's notation is adopted. If this system is applied to the 8825 Card Holder, there will be little information in this ratio with which to determine the energy correction factor. Figure 5.1 shows the ratio R_1/R_2 as a function of energy.

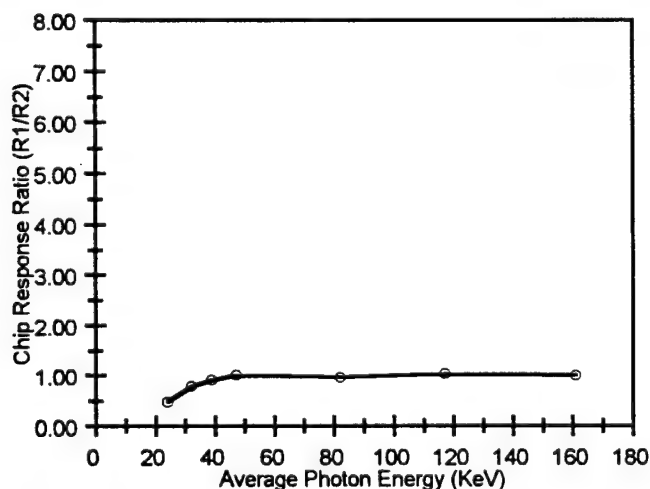


Fig 5.1 MCNP modeled response ratio R_1/R_2 versus average photon energy for the 8825 card holder. Only NIST H beams are used. There is very little photon energy discrimination in this ratio. The vertical axis range is large for consistency.

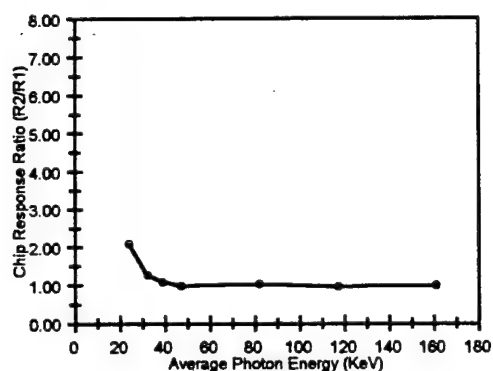
²⁸Cassata, Improved 62.

²⁹Cassata, Improved 63.

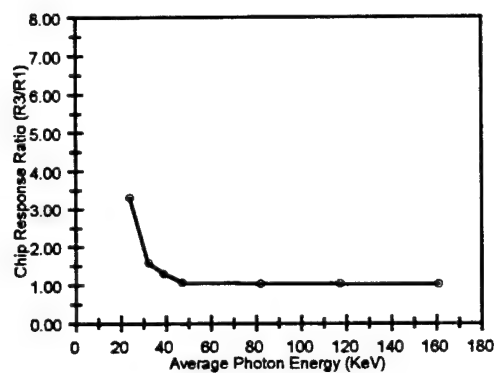
As shown in figure 5.1, between 40 and 160 KeV the response ratio of chip 1 to 2 is flat and it provides no information. This leads to a less accurate estimation of the $C(H_d)$ by the algorithm. The goal of the project was to improve this $C(H_d)$ so that R_1/R_2 had a greater energy dependence, therefore optimizing the card holder.

5.2 Analysis of the 8825 Energy Response

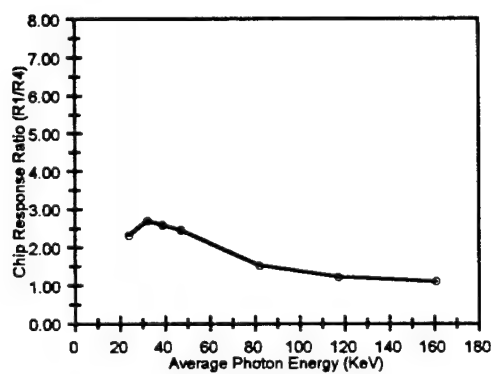
Because this model is interested in determining the energy response of the 8825 card holder, an energy spectrum that is nearly monoenergetic was used. The NIST H beams are the most nearly monoenergetic x-ray spectra that can be produced at NIST. For the remainder of this chapter, only the NIST H beams were used to model the energy response. The first step in the optimization process was to determine which chip ratios were applicable to improving the energy response. For the 8825 card holder, there are six possible permutations of chip ratios for 4 differently filtered chips. These ratios (R_2/R_1 , R_3/R_4 , R_1/R_4 , R_2/R_3 , R_2/R_4 , R_3/R_4) are shown in figures 5.2a through 5.2f as a function of average photon energy.



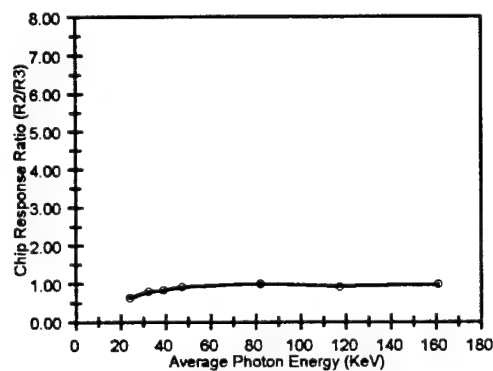
(a)



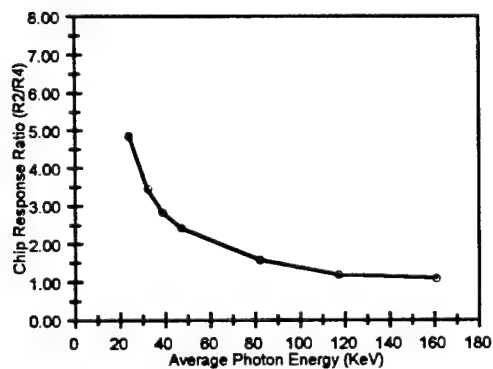
(b)



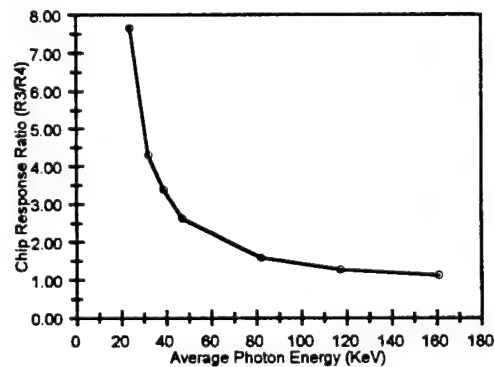
(c)



(d)



(e)



(f)

Fig 5.2 Six possible response ratios for the 8825 card holder. Each is a graph of a response ratio versus average photon energy.

These figures show that the ratio of R_2/R_4 and R_3/R_4 are best to use now for energy determination because of their dependence on photon energy. This finding was significant and will be helpful in improving the TLD reading algorithms for use by the NDC. Since the ratio R_3/R_4 had a similar photon energy dependence to R_2/R_4 and since R_3/R_1 was similar to R_2/R_1 , only R_2/R_1 and R_2/R_4 were used to determine photon energy. The ratios R_3/R_1 and R_3/R_4 may provide extra information for the algorithm, but are not necessary for optimization. The last two ratios, R_1/R_4 and R_2/R_3 , shown in figures 5.1c and 5.1d provide little energy information and were not examined further. The goal of the filter analysis was to obtain response curves which had a distinct value of energy for each ratio at low photon energies.

5.3 Filter Analysis

Two approaches were used to modify the card holder. The first was to vary the thickness of the existing 8825 card holder filters, copper (Cu) and tin (Sn). The second was to vary the filter material. In varying the filter material, metals of different atomic number were chosen so that their photon attenuation coefficients would be noticeably different.

In order to determine the optimum set of filter

materials and thickness, a figure of merit was developed for each set. A set of qualitative criteria for an optimized response was first determined so that a quantitative measurement could be assigned to a set of filters and materials. First, the ratios of a set of materials had to have a one to one correlation with average photon energy so they could be used in the algorithm. Second, the optimum curve of response ratio versus energy would have to be the closest to a 45 degree curve when the chip response ratio is plotted versus photon energy. A 45 degree curve would allow the best energy determination for a given ratio, and therefore, it was considered to be the ideal response curve.

Many methods were tested to assign a numerical value to the qualities mentioned above. The first method was to sum the absolute values of the slopes of the curves between each energy value. The card holder with the largest value would be the optimum design. The second method involved summing the sine of twice the angle of the slope between each energy value. Since the ideal slope is 45 degrees and since the slopes vary from zero degrees to 90 degrees, the sine of the twice the angle would vary from 0 to 1 and back to 0. The optimum card holder would once again have the highest value of the sum. Neither of these methods worked well because they gave results which did not agree with observed trends in the response curves. The last method involved finding

the area between the ideal and the actual curves. First, figure 5.3 gives a representation of the ideal 45 degree curve and a typical response.

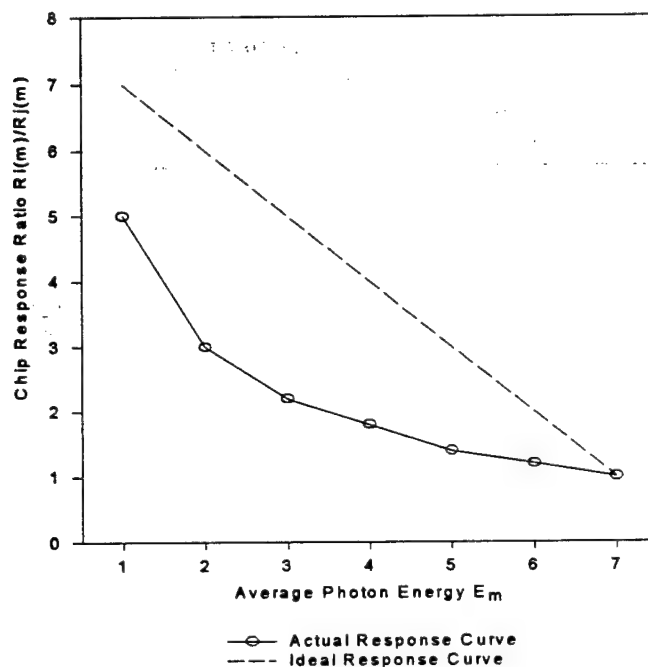


Fig 5.3 A typical response ratio and the ideal response ratio versus average photon energy. The vertical axis is the value of the ratio, and the horizontal axis is the average photon energy represented by an index, m , which corresponds to an energy in KeV. Each point is therefore labeled by indices i , j , and m .

E_m is the average photon energy where m varies from 1 to 7. Likewise, $R_i(m)/R_j(m)$ are the ratios for a corresponding value of m where i is 2 or 3 and j is 1 or 4. Using this notation, equation 5.3 gives the figure of merit (fom) for a particular set of filter materials and thickness.

$$fom = \sum_{i=2}^3 \sum_{\substack{j=1 \\ j \neq 2,3}}^4 (E_7 - E_1) \left(\frac{R_i(7)}{R_j(7)} + \frac{1}{2}(E_7 - E_1) \right) - \sum_{m=1}^6 \frac{1}{2}(E_{m+1} - E_m) \left(\frac{R_i(m)}{R_j(m)} + \frac{R_i(m+1)}{R_j(m+1)} \right) \quad (5.3)$$

This equation gives the total area between the actual and ideal curves for the various R_i/R_j produced by a card holder. The set of materials and thicknesses which has the smallest figure of merit is the optimum card holder. Table 5.1 gives the results of the analysis for the 8825 card holder. The first line of table 5.1 represents the current design of the 8825 card holder. The term N/A means that the response curves of the materials at that thickness were not functions of energy and therefore could not be used to calculate a figure of merit, nor could they be used in an algorithm. The range of thicknesses studied in this analysis were limited to the thickness of the front face of the 8825 card holder. Multiples of the original 8825 filter thicknesses were used for construction purposes.

Table 5.1 Figures of merit for various filter materials and filter thicknesses for the 8825 card holder. The combination of materials with the least figure of merit will be the optimum combination. The optimum values are highlighted in bold and italicized. The current values are underlined.

Filter Thickness (cm)					fom
$_{29}\text{Cu}$	$_{50}\text{Sn}$	$_{82}\text{Pb}$	$_{40}\text{Zr}$	$_{74}\text{W}$	
<u>.0102</u>	<u>.0584</u>				<u>37203</u>
.0204	.0584				37154
.0408	.0584				37092
.1000	.0584				37019
.2000	.0584				36976
<u>.0102</u>	<u>.0584</u>				<u>37203</u>
.0102	.0750				37182
.0102	.1168				37141
.0102		.0584			N/A
	.0584	.0102			N/A
	.0584		.0102		N/A
	.0584			.0102	37045
	.0584			.0500	N/A
	.0584			.1000	N/A

As shown in table 5.1 with bold entries, a combination of $_{29}\text{Cu}$ and $_{50}\text{Sn}$ are the optimum choices and are an improvement over the current design.

It was during this stage of the analysis that an error in the composition of the plastic filter was detected and corrected. The correction was small as it involved increasing the density thickness of the filter above chip 2. It did not invalidate any of the filter analysis modeling, and the relevant parts of the analysis were redone. The term "corrected" applies to the 8825 model after the

correction was made. Table 5.2 gives the results of the figure of merit analysis after the model correction was made. Again, the first line in table 5.2 represents the current 8825 design, while the bold entries represent the optimum filter thicknesses.

Table 5.2 Figures of merit for various filters materials and filter thicknesses for the 8825 card holder with the chip 2 filter correction. The combination of materials with the least figure of merit will be the optimum combination. The optimum values are highlighted in bold and italicized. The current 8825 values are underlined.

Filter Thickness (cm)		
²⁹ Cu	⁵⁰ Sn	fom
<u>.0102</u>	<u>.0584</u>	<u>37232</u>
.0204	.0584	37187
.0408	.0584	37131
.1020	.0584	37059
.1530	.0584	37033
<i>.2040</i>	.0584	<i>37018</i>
<u>.0102</u>	<u>.0584</u>	<u>37232</u>
.0102	.0750	37212
.0102	.1168	37170
.0102	<i>.1500</i>	<i>37157</i>
.0102	.1752	N/A
.0102	.2336	N/A

Hence, the optimum card holder is one that has a copper filter which is as thick as possible and a tin filter that is .1500 cm thick.

Finally, figures 5.4a and 5.4b show the improvement made to the response curves by this optimization analysis.

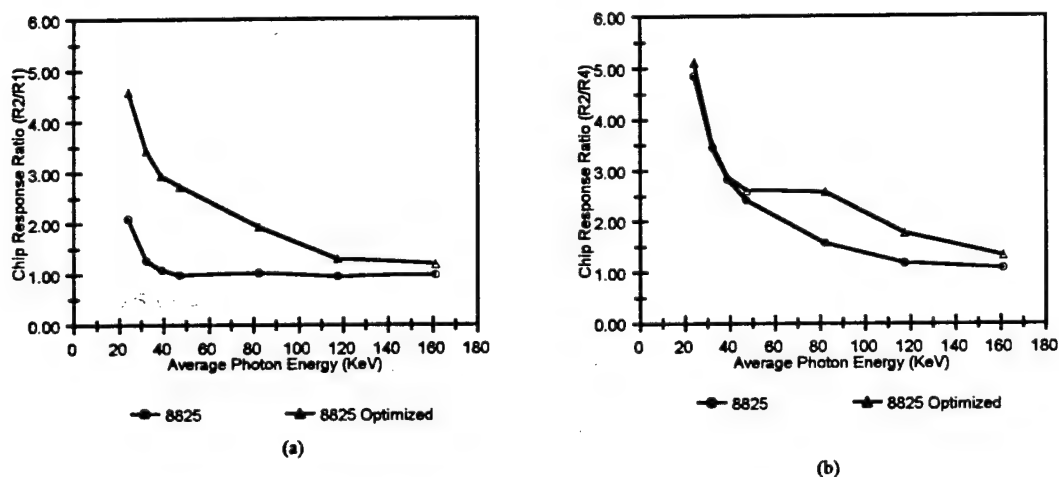


Fig 5.4 Response ratios R_2/R_1 and R_2/R_4 for the 8825 and optimized 8825 card holders versus average photon energy. In each case, the optimized curve is closer to the ideal 45 degree line.

As can be seen in figure 5.4, the optimized curve is significantly closer to the ideal 45 degree curve for R_2/R_1 , and slightly better for R_2/R_4 .

5.4 Conclusions on Filter Optimization

A methodology has been developed in this chapter to optimize the filter system for a dosimeter. First, model the response of the dosimeter to determine which chip ratios need modification. Second, vary the materials and material thickness used as filters in the model. Finally, determine which combination of filters has the lowest figure of merit. This chapter optimized the 8825 card holder with LiF thermoluminescent chips. The optimum configuration of

filters for the card holder are a copper filter 0.2040 cm thick, a PTFE filter, a Mylar filter, and a tin filter which is 0.1500 cm thick. This is different from the current design of the 8825 Card Holder which is not optimized to allow for photon energy determination. Chapter 6 will detail the next step of the project which was to construct the 8825I (8825 Improved) card holder. Chapter 7 then describes the experimental validation of the 8825I card holder.

Chapter 6: Improved Card Holder Construction

6.1 Design and Construction

With the 8825 Card Holder theoretically optimized for photon energy discrimination, the improved card holders had to be constructed. The goal of this section was to make a group of five prototype 8825 Improved (8825I) card holders at the Naval Academy for experimentation purposes. These prototypes were to be made as inexpensively as possible, but they still needed to demonstrate the properties that the improved card was designed to show.

The first obstacle was the quality of the materials that were to be used. Obtaining five copper and tin filters with the desired thickness which were of the same quality copper which is used in the card holder would have been difficult. Instead, filters from existing 8825 card holders were removed from existing holders and stacked to the desired thickness and used in the card holder. The card holders needed for this section were obtained from the Naval Dosimetry Center.

There were two constraints on the thickness of the improved filters. First, the improved filter thickness had to be a multiple thickness of a single filter and second, the filter had to fit inside the card holder retaining a reasonable amount of plastic on the front and back face of the card holder to contain the filter. For these reasons, a

copper filter which was 15 times the original thickness and a tin filter which was twice the original thickness were chosen.

In order to gain the desired filter thickness, some of the plastic holder had to be drilled away at the existing filter positions to accommodate the new filters. This also presented a problem. Different methods of removing the plastic were tested, but the final solution involved using a 1/2 inch end milling bit in a drill press to take out most of the plastic, and then using a Dremel Moto-Tool with various bits to grind the filter holes to the desired depth.

Figure 6.1 shows a representation of the 8825 and 8825I card holders. Each measurement given is accurate to within .003 cm.

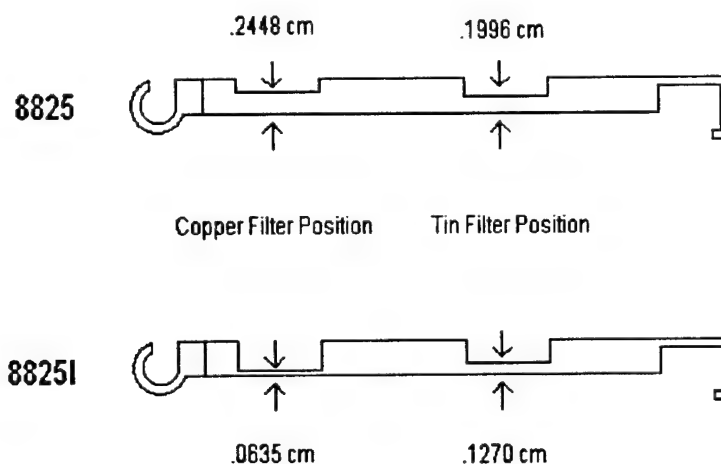


Fig 6.1 Differences in plastic filter thickness on the 8825 and 8825I card holders. In the 8825 card holder, the plastic thickness at the copper filter position was .2448 cm and at the tin filter position, .1996 cm. For the 8825I card holder the measurements were .0635 cm and .1270 cm respectively.

6.2 8825 and 8825I Card Holder Properties

Table 6.1 gives the density thicknesses of each of the filters used in the 8825 and 8825I card holder models. Density thickness is an important parameter in judging the filtration provided by a set of materials. Density thickness is defined as the density of a material times its thickness. To obtain the density thickness of a combination of materials in sequence, such as in this case where plastic is followed by a metal filter, the density thicknesses of the individual materials are added together.

Table 6.1 Density thicknesses of the filters in the 8825 and 8825I card holders. Each filter is numbered by the chip which it is over. Density thickness is in units of mg/cm².

Card Holder	Filters			
	1	2	3	4
8825	346	1013	7	631
8825I	1437	1013	7	985

As shown in Table 6.1, the density thickness of the filter position 1 which includes ABS plastic and copper has been increased by nearly five times and filter position 4 has increased by nearly 50%. This increase in density thickness allowed the card holder to produce the curves shown in figures 5.4a and 5.4b. With the construction of the improved dosimeter, another MCNP analysis was done to ensure that the 8825 and 8825I MCNP models correlated with experimental data. Chapter 7 covers the experimentation and the correlation of the data with the MCNP analysis.

Chapter 7: Experimental Verification of Filter Optimization

7.1 Experimentation

The goal of this section of research was to verify experimentally that the 8825I card holder was optimized for photon energy determination. Ideally, the experiments would have been performed at NIST using the H beams just as in the optimization, but the NIST x-ray facilities were not operational at the time of the experimentation, 2-6 February 1998. Instead, Armstrong Laboratories at Brooks Air Force Base, Texas provided the necessary facilities. Their Instrument Calibration Facility (ICF) had a J.L. Shepard 130 Ci ^{137}Cs Irradiator calibrated on 12 August 1997,³⁰ and a Seyfert Isovolt X-Ray Generator calibrated on 27 March 1997.³¹ The available beam codes for the x-ray generator were L100, M30, M50, M60, M100, M150, M250, M300, H150, and H300. A smaller set of these was used in the experimentation to maintain a consistent range of energies with the rest of the analysis.

The first part of the experimentation involved irradiating eight 8825 card holders and eight 8825I card holders with the ^{137}Cs source. Calibrated software was available at the ICF to determine the exposure time

³⁰Bruce B. Dicey, "Recalibration of J.L. Shepherd 130 Ci ^{137}Cs Irradiator" Memorandum, Armstrong Laboratory, Brooks AFB, 1997.

³¹Bruce B. Dicey, "Calibration of Seyfert Isovolt X-Ray Generator" Armstrong Laboratory, Brooks AFB, 1997.

necessary to irradiate the card holders to a dose of 150 mrem. Four TLD's were placed on the phantom at a time as shown in figure 7.1.

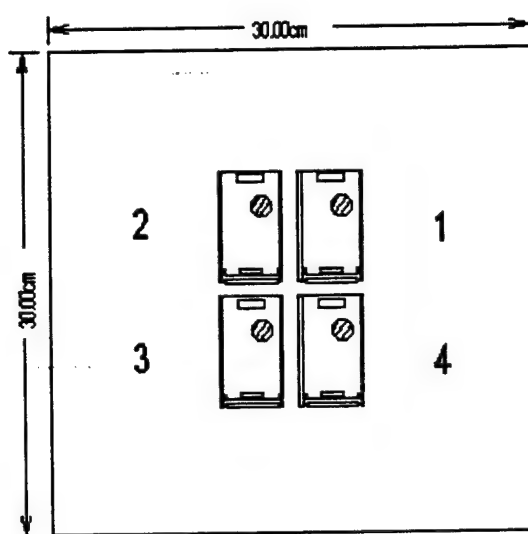


Fig 7.1 Experimental TLD configuration at the Instrument Calibration Facility using four card holders. The circles represent the mylar filter on the 8825 and 8825I card holders. The TLD's were placed on the phantom according to ANSI N13.11. Each position on the phantom was numbered one through four as shown.

The four TLD's were placed on the phantom according to the American National Standard for Dosimetry. Also, the front face of the phantom was placed at 195 cm from the ^{137}Cs source as modeled in the MCNP analysis and the phantom was centered with a laser centering device. ANSI N13.11 requires that the front face of the phantom be at least 1 m from the source.

Next, the exposure rates for the various x-ray beam codes were determined. This was done using a thimble type cavity ionization chamber called an Exradin Chamber. The

Exradin Chamber was calibrated at NIST on 13 May 1997.³²

The same procedures were used as detailed in the calibration report. Table 7.1 outlines the Seyfert Isovolt settings for each beam code and their corresponding dose rates at 2 m from the x-ray generator's tungsten target.

Table 7.1 Settings and dose rates for the Seyfert Isovolt X-Ray Generator at the Instrument Calibration Facility. Dose rates were measured at 2 m from the tungsten target on 3 February 1998.

Beam Code	Average Energy (KeV)	Filter	Voltage (KV)	Current (mA)	2 m Dose Rate (mrem/s)
L100	48	6	100	10	35.5
M60	34	1	60	5	7.68
M100	53	7	100	10	21.1
M150	73	8	150	10	32.8
H150	117	9	150	10	0.880

Before any data had been taken on 3 February, the x-ray generator was started according to one month start-up procedures, and thereafter, it was started according to daily start-up procedures.

Finally, irradiations were done of the TLD's using the x-ray generator. Two procedures were used. First, eight TLD's were irradiated using the 8825 card holder and then eight using the 8825I card holder for each beam code listed in table 7.1. The TLD's were placed on the phantom four at a time as in figure 7.1. In this case, the front face of the phantom was placed at 2 m from the tungsten target in

³²Paul J. Lamperti, "Report of Calibration" DG10160/97, Exradin Chamber, Model A3, Serial Number 158, 13 May 1997.

the x-ray generator, and the phantom was centered using a laser centering device. The second procedure involved placing TLD's one at a time on the center of the phantom face as in figure 7.2. Four TLD's using the 8825 card holder and four using the 8825I card holder were irradiated for each beam code in this manner.

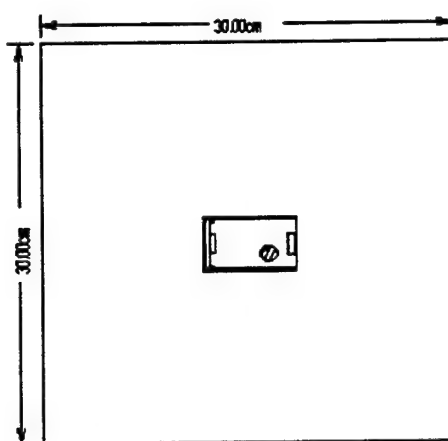


Fig 7.2 Experimental TLD configuration at the Instrument Calibration Facility using one card holder. The circles represent the mylar filter on the 8825 and 8825I card holders. The TLD's were placed on the phantom according to ANSI N13.11.

The type of 8801 card used in these experiments had the copper doped LiF chips. Control cards were used throughout the irradiation process. In all, 42 control cards were kept out of the irradiation. These control cards were used to calculate the background dose. Fade cards were also added to the group. Fade cards are cards which are given a known dose at a specific time to correct for the fading of the light signal after irradiating and prior to reading. These cards were not used in the final analysis though, because

the correction would have been less than one percent.

7.2 Data Analysis

The TLD's were read at the NDC on 6 February 1998 using a Harshaw 8800 reader. The reader gives output in terms of mrem by dividing the light output (LO) by the reader calibration factor (RCF). The ECC's for each chip on each card was determined using the ECC machine at the NDC. The ECC's were then multiplied by the reader's output as given by equation 2.6 to obtain a dose for each chip. Finally, the average dose on the control cards was subtracted from the dose on the irradiated cards to find the experimental ODDE.

While analyzing the data, it was noticed that there was a positional bias in the TLD's which were placed on the phantom four at a time. Phantom position 3 as shown in figure 7.1 was consistently receiving the highest doses while phantom position 1 was receiving the lowest. Because of this bias, the cards which were centered on the phantom were treated separately from the cards which were irradiated four at a time.

In order to show the phantom positional bias clearly for the four card irradiations, the dose received by each TLD is summed over all the irradiations. If each dosimeter were receiving equal amounts of dose over all the

irradiations then the sum of the doses in a TLD should be equal at all phantom positions. Figure 7.3 shows this using the total dose given to a TLD at each position on the phantom.

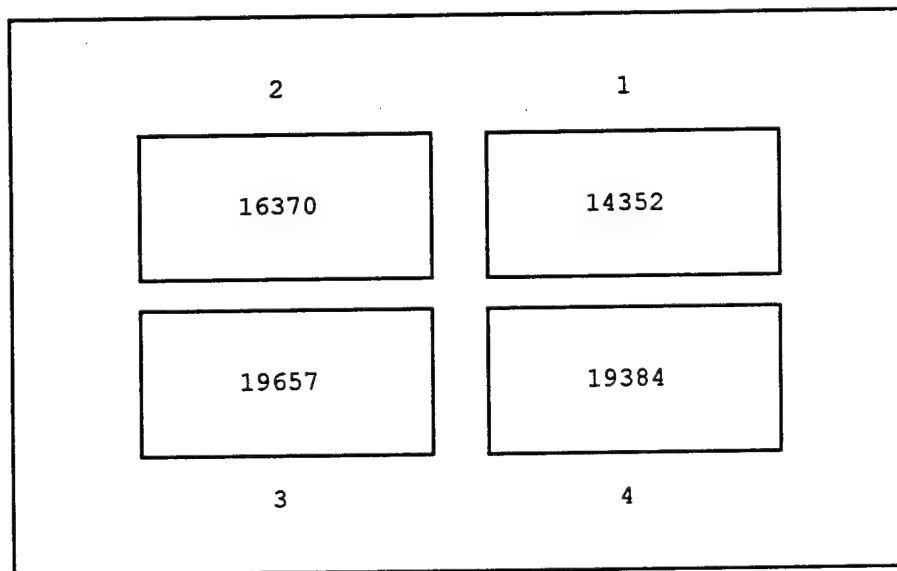


Fig 7.3 The TLD total dose over all irradiations at each phantom position. The large outer box represents the phantom, while the small inner boxes represent the individual TLD's. There are four phantom positions, each numbered on the figure. The numbers within the TLD boxes have units of mrem.

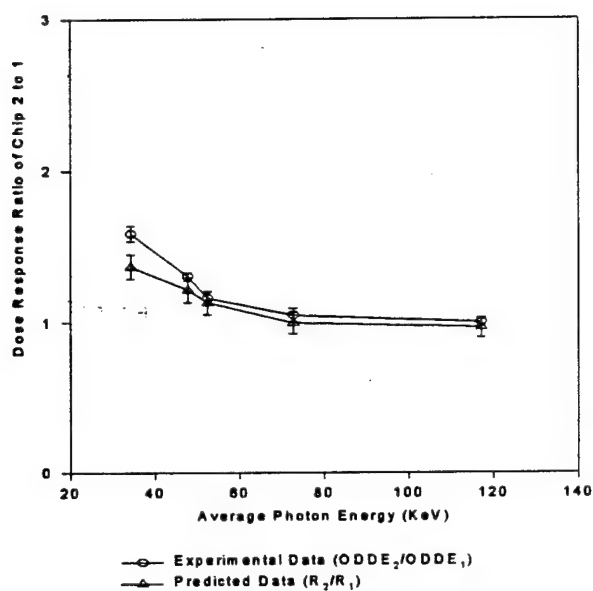
Further examination of Figure 7.3 shows the positional bias. There are a number of potential explanations for this bias. First, the beam may have not have been centered with the laser sight. Second, the beam may have been centered without being uniform across the phantom. Neither possibility can be confirmed by this experimental data.

Since the total dose at each chip position was known and it was also known that they should be equal, this

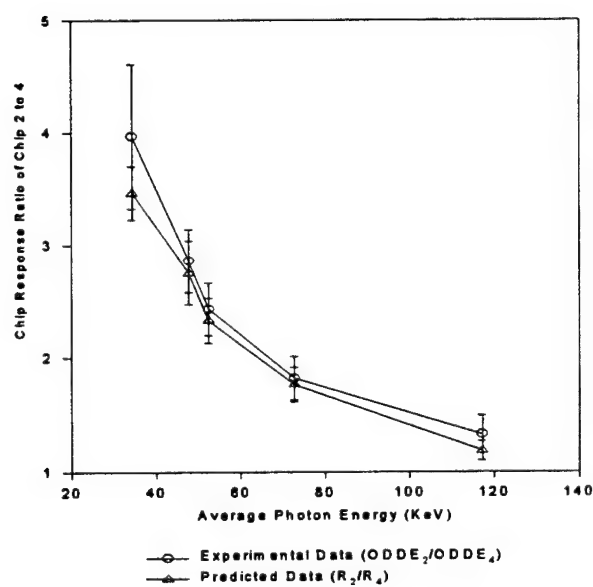
positional bias was removed by dividing by an unbiasing factor. The unbiasing factor was found by dividing the total dose at a chip for a certain phantom position by the total chip dose for all four phantom positions. With this done, the data looked as if the beam had been centered and uniform across the four TLD's. Next the various response ratios were computed both for the data from the centered cards and for the data from the unbiased cards. Finally, the two sets of data were combined to constitute the plotted values for the experimental data shown in the next section.

7.3 Correlation of MCNP Model with Experiment

Figures 7.4 and 7.5 compare the experimental and modeled results for both the 8825 and 8825I card holders respectively. Only the results of the ratios R_2/R_1 and R_2/R_4 will be discussed since they have been found to be the most important for optimization as shown in the discussion of figure 5.2.

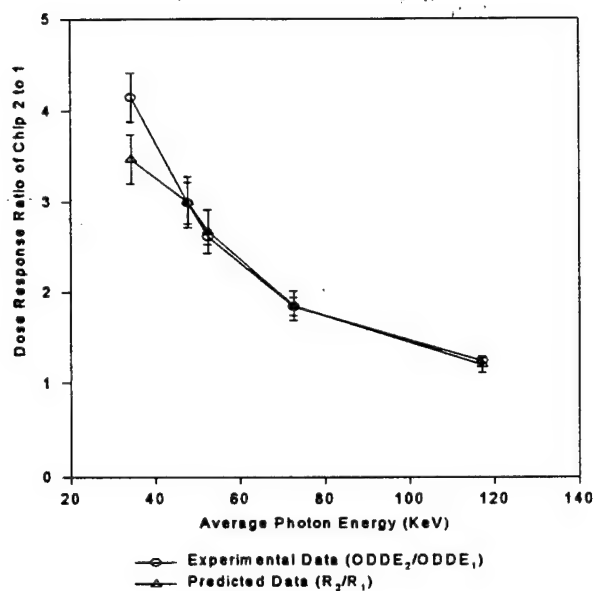


(a)

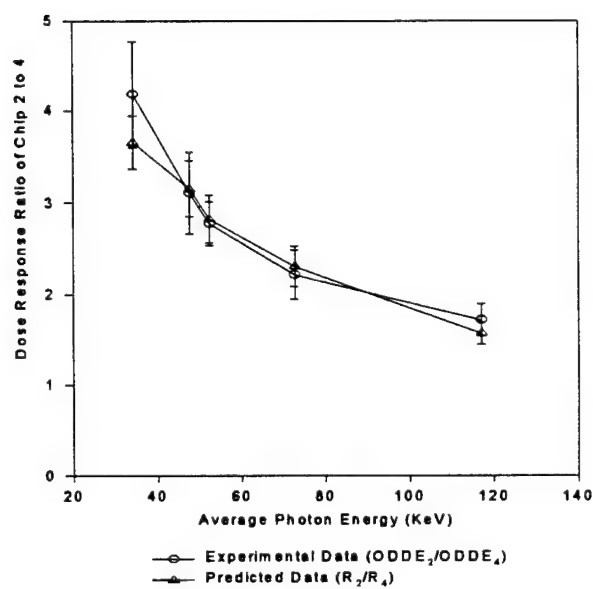


(b)

Fig 7.4 Comparison of the response ratios of the experimental data to the modeled data for the 8825 card holder. Figure 7.4a shows the response ratio of chip 2 to 1 while 7.4b shows chip 2 to 4. The error bars represent two standard deviations.



(a)



(b)

Fig 7.5 Comparison of the response ratios of the experimental data to the modeled data for the 8825I card holder. Figure 7.5a shows the response ratio of chip 2 to 1 while 7.5b shows chip 2 to 4. The error bars represent two standard deviations.

As shown in figures 7.4 and 7.5, the experimental data falls within two standard deviations of the predicted MCNP data on all data points except for 34 KeV (M60) for the ratio of chip 2 to 1. This close agreement between the experimental results and the MCNP model was strong evidence of the correctness of the MCNP model as well as assumptions made in the analysis. Because the data in figures 7.4b and 7.5b correlated with the modeled data, the figure of merit calculation done in Chapter 5 applies to the experimental data. The figure of merit calculations show that the response of the 8825I card holder was improved in the ratios R_2/R_1 and R_2/R_4 compared to the 8825. The final step, discussed in Chapter 8, was to recommend an improved card holder for use by the Naval Dosimetry Center.

Chapter 8: Recommendations for a New Card Holder

There were several requirements which were taken into consideration when developing a final recommendation for the Navy's card holder including two requirements which had not been considered up to this point. First, the card holder had to provide information about three different types of dose: deep, shallow, and eye dose. The deep dose is equivalent to the amount of dose received by human tissue at a depth of 1 cm. One centimeter of tissue has a density thickness of 1000 mg/cm^2 . The shallow dose is the amount of dose received by tissue at a depth of 0.007 cm and it corresponds to a density thickness of 7 mg/cm^2 . The final dose is the eye dose which is the amount of dose received by a human eye. That filtration corresponds to a density thickness of 300 mg/cm^2 . The second requirement was that one of the LiF chips respond in a tissue equivalent manner so that the $C(H_d)$ for that chip was nearly one. This would allow one chip to give an estimation of the dose without applying a correction factor. The final requirement was that at least one chip ratio have improved photon energy determination over the current (8825) card holder.

Considering these criteria, the 8825P (8825 Proposed) card holder was then designed. Table 8.1 summarizes the three card holders, their filters, and their density thicknesses.

Table 8.1 Summary of the current, improved, and proposed card holders. The filter material is followed by the density thickness at that chip in parenthesis with units of mg/cm^2 . The density thicknesses are from the modeled values. Each chip position except position 3 includes ABS plastic in the density thickness.

Card Holder	Chip Position			
	1	2	3	4
8825	Cu (346)	PTFE (1013)	Mylar (7)	Sn (631)
8825I	Cu (1437)	PTFE (1013)	Mylar (7)	Sn (985)
8825P	Cu (346)	PTFE (1013)	Mylar (7)	Cu (1437)

As shown in table 8.1, this design process resulted in a card holder that is the same as the current 8825 design except that the tin filter over chip 4 was replaced by a copper filter. The filters at chip 2 and 3 were not changed from the original 8825 design because they provided the deep and shallow dose filtrations respectively. The filter at chip 1 was not changed for two reasons. First, the filtration on that chip was already $300 \text{ mg}/\text{cm}^2$ fulfilling the eye dose requirement. Second, this chip has a $C(H_d)$ factor which is close to unity which fulfills another requirement for this chip. Figure 8.1 shows the $C(H_d)$ factor for chip 1 as a function of photon energy. The $C(H_d)$ factor was calculated from the experimental data collected at the ICF using equation 5.2.

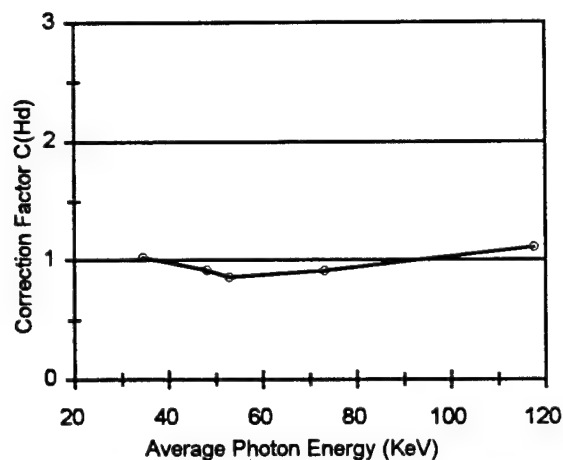


Fig 8.1 Correction factor $C(H_d)$ versus average photon energy for chip 1 of the 8825P card holder. Chip 1 is filtered by a copper filter 0.0102 cm thick and ABS plastic for a total filtration of 300 mg/cm².

The correction factor for chip 1 is within 15% of unity for photon energies between 20 and 120 KeV. Applying equation 5.1 allows the ODDE from chip 1 to be used to estimate the CDDE without applying the correction factor for low energies. The reason that the copper filtered chip 1 will have a unity $C(H_d)$ response versus photon energy can be explained as follows. Unfiltered LiF over responds to low photon energies, but the addition of the thin copper filter attenuates most of the low energy photons. This addition allows chip 1 to have an approximately tissue equivalent response ($C(H_d) \approx 1$).

Finally, the filter at chip 4 was changed to copper with a thickness of 0.1530 cm, providing a density thickness of 1437 mg/cm². This copper filter thickness (0.1530 cm,

fom=37033) had a lower figure of merit than the 8825 tin filter (0.0584 cm, fom=37232) and the optimized tin filter (0.1500 cm, fom=37157). These figures of merit are taken from table 5.2. The lower figure of merit indicates that the copper filter will provide a better photon energy determination than the 8825 tin filter or an optimized tin filter.

Next, equations that can be used to estimate photon energy given a response ratio were developed. These equations were the result of performing various transforms on the modeled response of the 8825P card holder to find the curve which had the highest coefficient of determination (R^2). Since the MCNP model had been shown to agree well with experimental data, the following equations should apply to the actual response of the 8825P card holder. This is significant because this analysis may remove the need to perform costly and time consuming experimental irradiations. Figures 8.2, 8.3, and 8.4 give the correlated response of photon energy versus R_2/R_1 , R_2/R_4 , and R_3/R_4 for the 8825P card holder. Equations 8.1, 8.2, and 8.3 are the results of regression analyses to the data in these curves.

Figure 8.3 gives the modeled response ratio R_2/R_4 for the 8825P card holder.

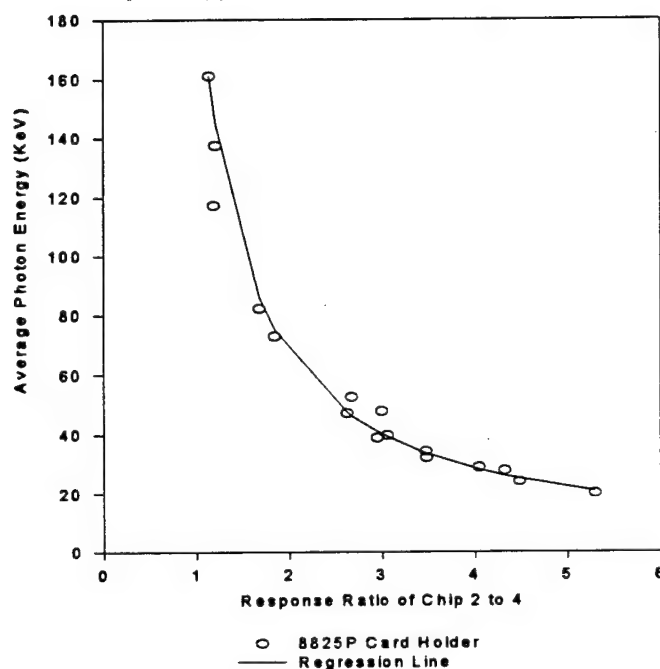


Fig 8.3 Modeled average photon energy as a function of response ratio of chip 2 to 4 for the 8825P card holder. Various beam codes are used in this analysis: M30, H30, L50, M50, H40, M60, H50, L80, H60, L100, M100, M150, H100, H150, M250, and H200. The equation of the regression line is found in equation 8.2.

Equation 8.2 gives an empirical relationship between the response ratio R_2/R_4 and photon energy in KeV based on a curve fit to the data. The coefficient of determination (R^2) for this regression is 0.98.

$$E = \frac{1}{a\left(\frac{R_2}{R_4}\right) + b} \quad (KeV)$$

$$a = 0.0100$$

$$b = -5.23 \times 10^{-3} \quad (8.2)$$

$$1.14 \leq \frac{R_2}{R_4} \leq 5.23, 162 \geq E \geq 20.9$$

Finally, figure 8.4 gives the modeled response ratio R_3/R_4 for the 8825P card holder versus photon energy.

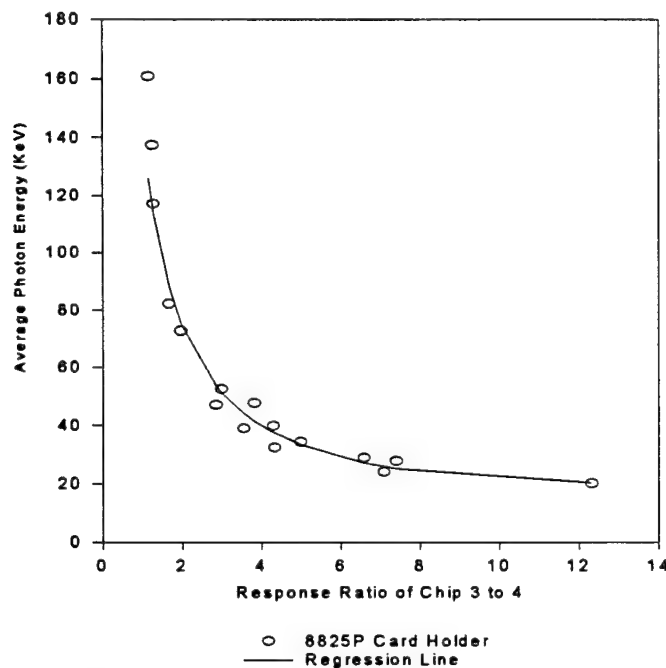


Fig 8.4 Modeled average photon energy as a function of response ratio of chip 3 to 4 for the 8825P card holder. Various beam codes are used in this analysis: M30, H30, L50, M50, H40, M60, H50, L80, H60, L100, M100, M150, H100, H150, M250, and H200. The equation of the regression line is found in equation 8.3.

Equation 8.3 gives an empirical relationship between the response ratio R_3/R_4 and photon energy in KeV based on a curve fit to the data in figure 8.4. The coefficient of

determination (R^2) for this regression is 0.97.

$$E = \frac{1}{a\left(\frac{R_3}{R_4}\right)^2 + b\left(\frac{R_3}{R_4}\right) + c} \quad (KeV)$$

$$a = -2.78 \times 10^{-4}$$

$$b = 7.46 \times 10^{-3}$$

$$c = -3.65 \times 10^{-4}$$

$$116 \leq \frac{R_3}{R_4} \leq 12.31, 125 \geq E \geq 20.3$$
(8.3)

Equations 8.1, 8.2, and 8.3 can be used in the reading algorithm for TLD's using the 8825P card holder. Using all three equations will allow the reading algorithm to estimate the photon energy more accurately in regions where the energy ranges overlap. A more accurate estimate of the $C(H_d)$ is also possible due to the increased response over the 8825 card holder for photon energy determination. If only one ratio can be used as in the current reading algorithm, the ratio of chip 2 to 4 should be used since it covers the largest range of energies compared to the other chip ratios.

There has been some research which suggests that the ratios R_2/R_1 and R_2/R_4 may be double valued at higher energies for the 8825 card holder.³³ John Chase, from Ontario Hydro, suggested that at energies above 162 KeV the ratio R_2/R_4 had a response ratio greater than the 162 KeV

³³W. John Chase, "Ontario Hydro Design and Type Testing Results for the Harshaw 8828 Card Holder," Presentation at Harshaw User's Symposium (San Diego) March 1998.

response ratio. If the response ratio curve were double valued at higher energies, a distinct photon energy could not be found from a particular response ratio. This claim lead to a further examination of the data from the ICF.

The ICF data supported the Ontario Hydro Data for the 8825 card holder. The 662 KeV photon energy had an R_2/R_4 value great than the 162 KeV value. Thus, the 8825 card holder is double valued over the photon energy range of 20 KeV to 662 KeV. Conversely, the 8825I card holder data showed that the values for R_2/R_1 and R_2/R_4 continued to decrease with increasing photon energy up to 662 KeV. Therefore, the 8825I card holder had the desirable monotonic photon energy response. Consequently, algorithms using the 8825I or the 8825P card holder do not have a double valued function problem for energies above 160 KeV. This is a significant improvement in photon energy determination over the 8825 card holder.

Chapter 9: Conclusions

9.1 Conclusions

Overall, this research has been successful at developing a new card holder with improved photon energy determination characteristics. This new card holder will be better able to meet NVLAP criteria than the previous card holder due to the improved accuracy of the calculated dose in the dosimeter reading algorithm. There were many steps in this analysis. First, theoretical calculations were compared with experimental data of the 8802 card holder. Then the MCNP model of the 8802 card holder was created and compared with the experimental data. Next, the 8825 card holder was optimized for photon energy determination using the MCNP program. The MCNP models of the 8825 and 8825I card holders were compared with experimental data taken at Armstrong Laboratories. Finally, a card holder which met certain NDC requirements and which was improved in photon energy determination over the 8825 card holder was recommended for use by the NDC.

Many important results were developed in this research. First, theoretical calculations were performed on the energy deposited in the LiF in the 8802 card holder. These calculations were within 20% of the experimental data. This analysis confirmed that light output was proportional to the energy deposited in a material. It also suggested that a

more detailed analysis would improve the correlation with experiment.

Energy deposition calculations in the 8802 card holder were then performed using the MCNP program. The first model had a large relative error and a lengthy run time. Many techniques were then applied to the model to improve the correlation with experiment including removing unnecessary parts of the model, employing MCNP error reduction techniques, and removing electron transport from the problem. The alterations made to the original model were significant for future modeling. The most significant finding in this stage of the project was that electron energy deposition did not significantly contribute to the light output because of the low dopant concentration and the short mean free path of the electron in LiF. The MCNP modeled data fell to within two standard deviations of the experimental response for the 8802 card holder.

An MCNP model of the 8825 card holder was created using the techniques developed in the modeling of the 8802 card holder. Then different filter materials and thicknesses were modeled in the 8825 card holder to find the optimum configuration for photon energy determination. A figure of merit which could be assigned to a certain filter combination was also developed and the optimum configuration for photon energy determination was found. This process was

also significant because the photon response of other dosimetry systems can also be optimized in this manner. The card holder which had the optimized filter configuration, the 8825I card holder, was then constructed.

Irradiations were performed at Armstrong Laboratories at Brooks AFB, Texas on the 8825 and 8825I card holders using the 8801 card with copper doped LiF. The data from these irradiations was collected at the NDC using their Harshaw reading equipment. This experimental data also fell within two standard deviations of the MCNP model for both card holders. This analysis confirmed that the MCNP modeling methodology approximated experimental conditions and that the photon energy response of the 8825I dosimeter had been improved over the 8825.

Finally, a new card holder design was recommended to the NDC for use by the U.S. Navy. This card holder was not completely optimized for photon energy determination, but it used the results of the optimization analysis to improve its photon energy response over the previous (8825) model. Equations were then developed which fit the MCNP modeled response. These equations could be used in the reading algorithm to determine the average energy of the irradiating photons, and hence assign a more accurate dose value to the exposure received by the individual who wore the TLD.

9.2 Recommendations for Further Research

There are many areas which could be studied further before implementing this card holder. First, the card holder must be characterized for neutron and beta response. This should be done with several different neutron and beta sources. NIST has thermal neutron sources, ^{252}Cf fission neutron sources, and ^{90}Sr beta sources and the U.S. Naval Academy has a 14 MeV neutron source. Additionally, the performance of the card holder in mixed fields, combined neutron and gamma fields, should be studied. More research should also be conducted in the area of electron energy deposition in the LiF chips in order to bring the MCNP model and experiment into closer agreement. Since the filter thickness has been increased, a study of the angular dependence of the TLD could be undertaken. The TLD's response to higher energy photons could also be studied in the range from 160 to 1340 KeV to address the research done by Ontario Hydro mentioned in Chapter 8. Finally, TLD reading algorithms based on the equations developed in Chapter 7 should be developed. These equations could also be used in conjunction with neural networks as proposed by LT Cassata.³⁴ With this study and continued research, the accuracy of the NDC's dosimetry will continue to improve to meet the stricter NVLAP requirements.

³⁴Cassata, Improved.

Bibliography

- American National Standard for Dosimetry. "Personnel Dosimetry Performance - Criteria For Testing." HPS N13.11-1993.
- Brandup, J. Polymer Handbook. New York: Wiley, 1989.
- Briesmeister, Judith F. MCNP - A General Monte Carlo N-Particle Transport Code. Version 4B. LA-12625-M 1997
- Brydson, J.A. Plastic Materials. London: Newnes, 1975.
- Cassata, James R., D.A. Shauer, M.E. Nelson, G.A. Pertmer, and G.K. Riel. "Impact of the revised ANSI Standard on Accredited Thermoluminescence Dosimeter Processors." Radiation Protection Dosimetry, Vol. 67, No. 3, pp. 167-177, 1996.
- Cassata, James R. Improved Personnel Dosimetry Using Copper Doped Lithium Fluoride Thermoluminescent Dosimeters and Neural Network Algorithms. diss., U. of Maryland, Ann Arbor: UMI, 1997.
- Cember, Herman. Introduction to Health Physics. New York: McGraw, 1996.
- Chase, W. John. "Ontario Hydro Design and Type Testing Results for the Harshaw 8828 Card Holder." Presentation at Harshaw User's Symposium, San Diego, March 1998.
- Dicey, Bruce B. "Calibration of Seyfert Isovolt X-ray Generator." Armstrong Laboratory, Brooks AFB, 1997.
- Dicey, Bruce B. "Recalibration of J.L. Shepherd 130 Ci ¹³⁷Cs Irradiator." Memorandum. Armstrong Laboratory, Brooks AFB, 1997.
- Grigonev, Igor. Handbook of Physical Quantities. New York: CRC Press, 1997.
- Harper, Charles A. Handbook of Plastics and Elastomers. New York: McGraw, 1975.
- Hollenbeck, William H. Radiation Protection. Boca Raton: Lewis, 1994.
- Horowitz, Y.S. "LiF:Mg,Ti versus LiF:Mg,Cu,P: The Competition Heats Up." Radiation Protection Dosimetry, Vol. 47 No. 1/4, pp 135-141, 1993.

- Hubbell, J.H. and S.M. Seltzer. "Tables of X-Ray Mass Attenuation Coefficients and Mass Energy Absorption Coefficients." NIST, 1995.
- Hughes, Grady H. "Treating Electron Transport in MCNP."
- ICRU Report 26. "Neutron Dosimetry for Biology and Medicine."
- ICRU Report 33. "Radiation Quantities and Units."
- Iles, W.J. "The Computation of Bremsstrahlung X-Ray Spectra Over An Energy Range 15 KeV to 300 KeV." National Radiological Protection Board
- Jaeger, Thomas. Principles of Radiation Protection Engineering. Trans. Dr. Dresner. New York: McGraw, 1965.
- Lamperti, Paul J. Calibration of X-Ray and Gamma-Ray Measuring Instruments. NBS Special Publication 250-16, 1988.
- Lamperti, Paul J. "Report of Calibration" DG10160197, Exradin Chamber, Model A3, Serial Number 158, 1997.
- Lux, Ivan. Monte Carlo Particle Transport Methods. Boston: CRC Press, 1991.
- Seltzer, Stephen M. "Calculation of Photon Mass Energy-Transfer and Mass Energy Absorption Coefficients." Ionizing Radiation Div, NIST.
- Shapiro, Jacob. Radiation Protection. Cambridge: Harvard Press, 1981.
- Soares, C.G. "Spectral Files" diskette, NIST.
- Soares, C.G. and M Ehrlich. "Comparison of NIST and ISO Filtered Bremsstrahlung Calibration Beams." Ionizing Radiation Div., NIST.
- United States, Naval Sea Systems Command. Radiological Affairs Support Program Manual. NAVSEA S0420-AA-RAD-010, 1991.
- Zha, Z. "Preparation and Characteristics of LiF:Mg,Cu,P Thermoluminescent Material." Radiation Protection Dosimetry, Vol. 47, No 1/4 pp. 111-118, 1993.

Appendix A: Card Holder Materials

The following materials were used in modeling the 8802, 8825, and 8825I card holders. In order to model a material in MCNP, the percent by mass of the constituent elements and the material density must be known. The following is a list of each composite material, its constituent element, and its density.

ABS - Acrylonitrile Butadiene Styrene^{35,36,37}

H	8.9%
C	82.7%
N	8.4%

1.04 g/cm³

Mylar - Polyethylene Terephthalate³⁸

H	4.2%
C	62.5%
O	33.3%

1.45 g/cm³

PTFE - Polytetrafluoroethylene³⁹

C	24.0%
F	76.0%

2.08 g/cm³

³⁵Charles A. Harper, Handbook of Plastics and Elastomers, (New York: McGraw, 1975) 1-62.

³⁶J.A. Brydson, Plastic Materials, (London: Newnes, 1975) 365.

³⁷Igor Grigonev, Handbook of Physical Quantities, (New York: CRC, 1997)

³⁸J. Brandup, Polymer Handbook, (New York: Wiley, 1989) V/101.

³⁹ICRU Report 26, "Neutron Dosimetry for Biology and Medicine," (Bethesda, 1976) 91.

PMMA - Polymethyl Methacrylate⁴⁰

H	8.0%
C	60.0%
N	32.0%

1.20 g/cm³

TLD-700⁴¹

Li	27.04%
F	72.96%

2.63 g/cm³

TLD-600⁴²

Li	24.13%
F	75.87%

2.63 g/cm³

Air (Dry)⁴³

N	75.5%
O	23.2%
Ar	1.3%

0.002 g/cm³

⁴⁰ICRU Report 26, 91.

⁴¹Harshaw Bicron Corporation

⁴²Harshaw Bicron Corporation

⁴³ICRU Report 26, 92.

Appendix B: NIST Beam Codes

The following table is a list of the NIST beam codes that appear in this research and their experimental calibration conditions.

Table B.1 NIST beam codes and their calibration conditions that are used in this research. N/A means not available.

Beam Code	Average Energy (KeV)	Voltage (KV)	Current (mA)
L50	28	50	N/A
L80	40	80	N/A
L100	48	100	10
M30	20	30	7.5
M50	29	50	10
M60	34	60	5
M100	53	100	10
M150	73	150	10
M250	139	250	10
H30	24	30	N/A
H40	33	40	N/A
H50	39	50	N/A
H60	47	60	N/A
H100	83	100	N/A
H150	117	150	10
H200	162	200	N/A

Figures B.1, B.2, and B.3 show graphs of the various spectra used in the analysis. These spectra were obtained from NIST. They include the photon energy and the relative number of photons found at that energy. These spectra were used in the MCNP program to model the photon energy.

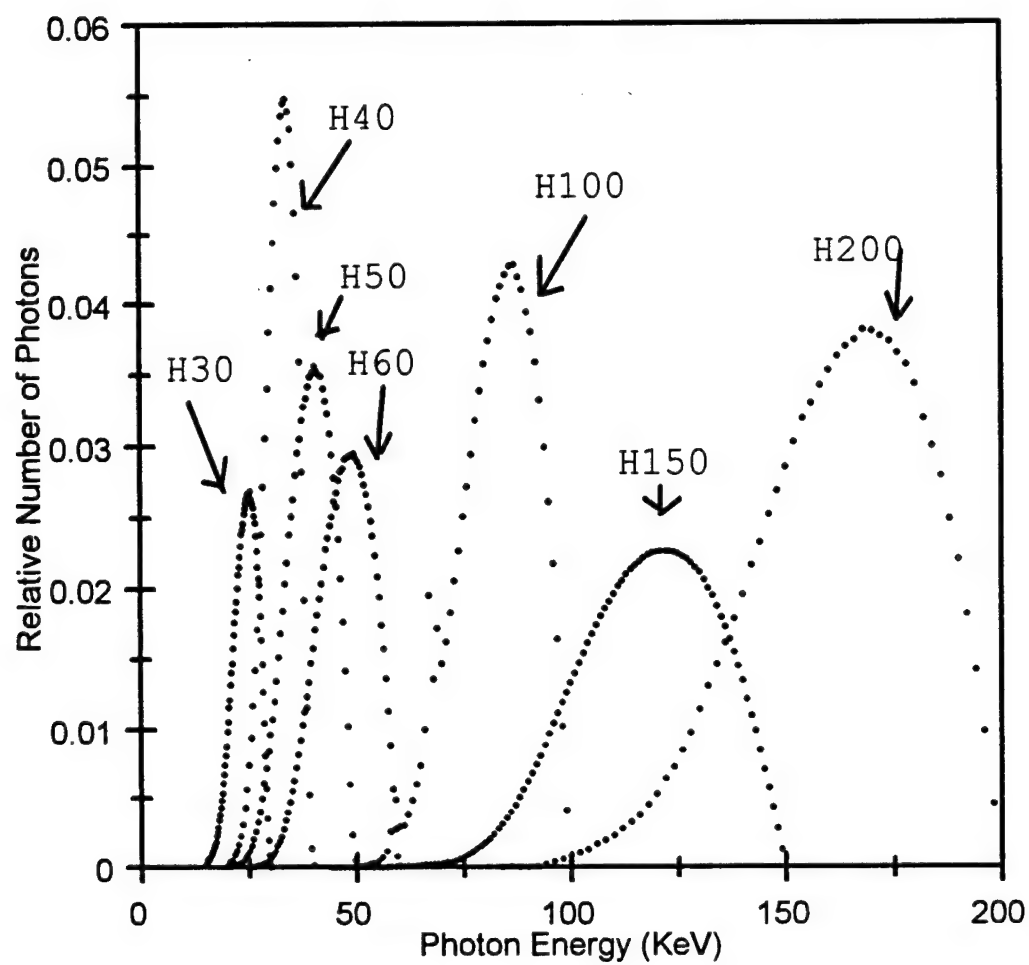


Fig B.1 Relative number of photons versus photon energy for the NIST heavily filtered (H) beams.

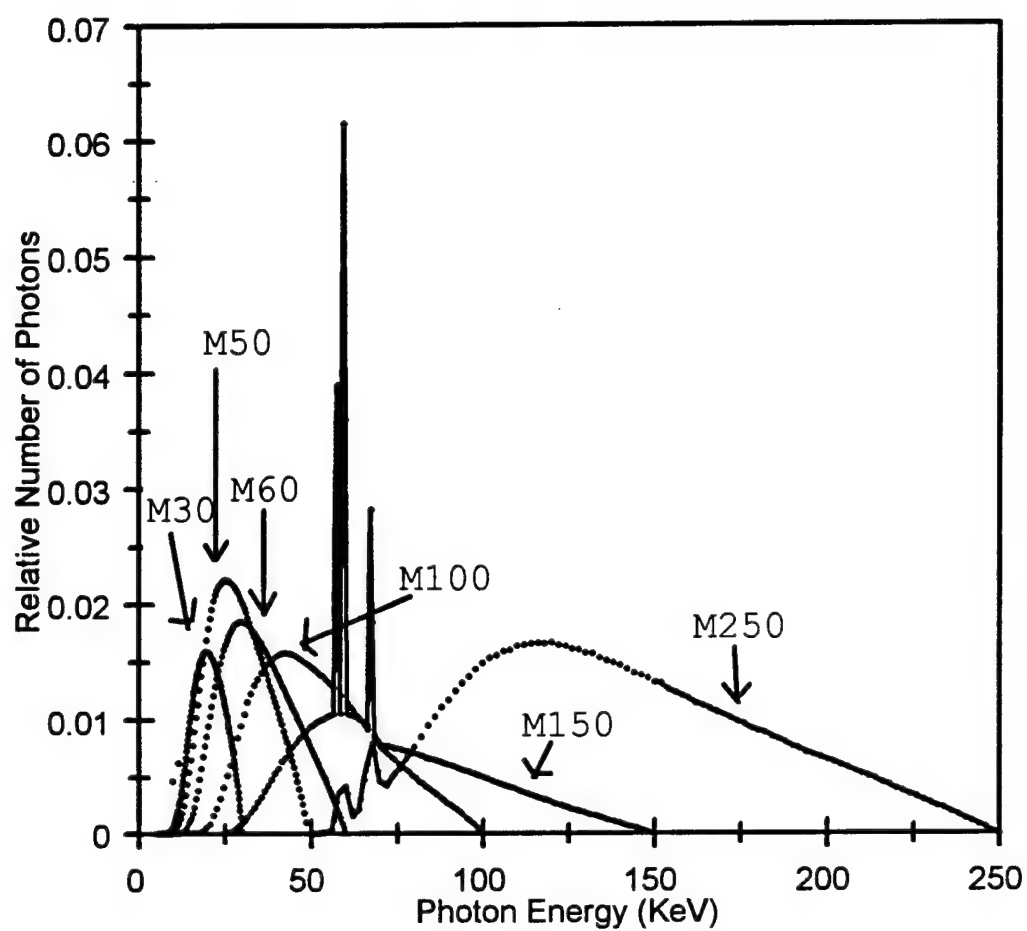


Fig B.2 Relative number of photons versus photon energy for the NIST medium filtered (M) beams.

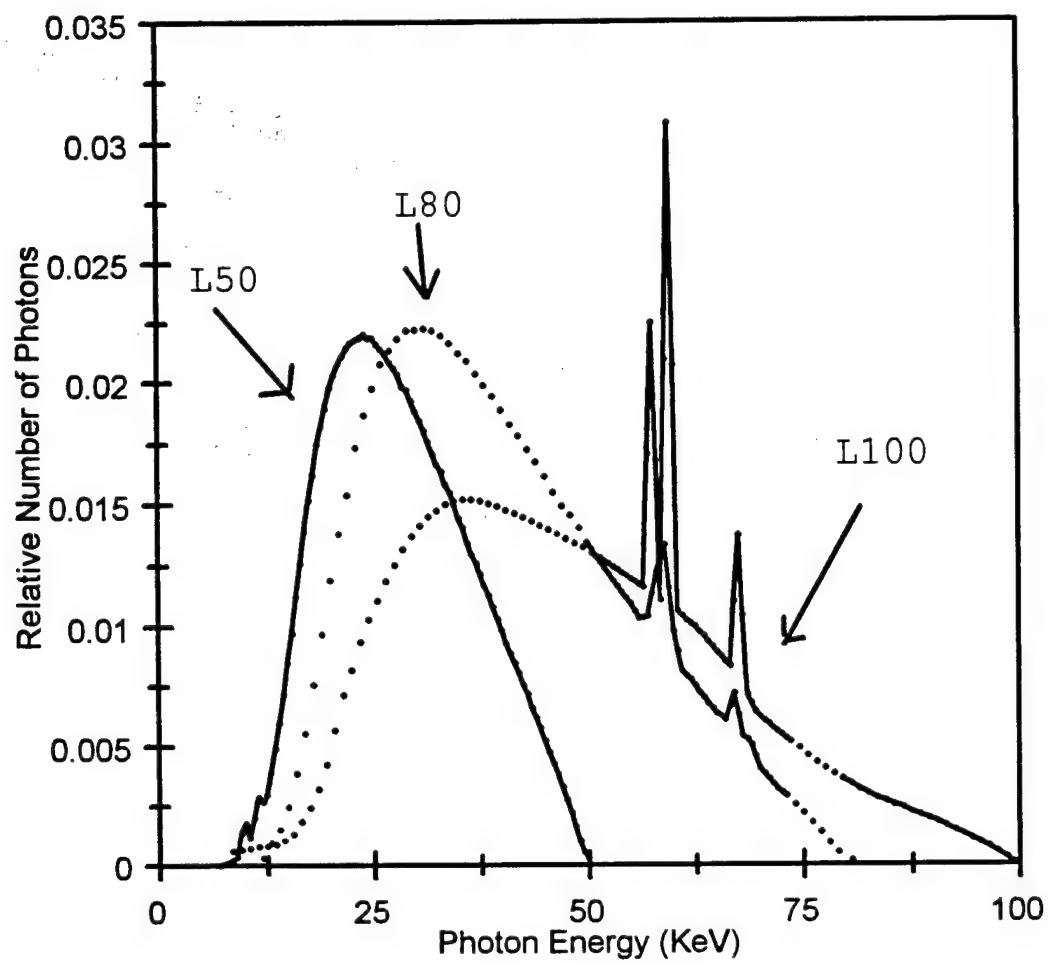


Fig B.3 Relative number of photons versus photon energy for the NIST lightly filtered (L) beams.

Appendix C: MCNP Input Files

The following are the input files used for the MCNP for the 8802, 8825, and 8825I card holders. Each line in the input file is called a card. The c cards, or comment cards, preface each section of code with its purpose. The cell descriptions use the surfaces defined in the surface description to build areas in space filled with the various materials. The mode card sets this problem for photon transport. The importance card has a number corresponding to the photon importance in each cell. The SDEF, SI, and SP cards are all used to define the photon source. The *F8 cards tally the energy deposited in a cell. The M cards define the composition of a material, and finally, the NPS card sets the number of particles modeled.

C.1 8802 Card Holder MCNP Input File

```
c 8802 Card Holder
c Cell Descriptions
1 1 -8.96 3 -4 -24 $ copper chip
2 2 -1.45 3 -4 -25 $ mylar filter
3 3 -2.63 5 -7 11 -12 17 -18 $ chip 1 TLD-700
4 3 -2.63 5 -7 11 -12 19 -20 $ chip 2 TLD-700
5 3 -2.63 5 -6 13 -14 19 -20 $ chip 3 TLD-700
6 4 -2.63 5 -7 13 -14 17 -18 $ chip 4 TLD-600
7 5 -2.699 4 -8 10 -15 16 -21 22 23 25 26 $ Aluminum
8 6 -.002 -22 4 -8 (-5:7:-11:12:-17:18) $ Air around chip1
9 6 -.002 -23 4 -8 (-5:7:-11:12:-19:20) $ Air around chip2
10 6 -.002 -25 4 -8 (-5:6:-13:14:-19:20) $ Air around chip3
11 6 -.002 -26 4 -8 (-5:7:-13:14:-17:18) $ Air around chip4
12 6 -.002 -24 2 -3 $ Air above copper
13 6 -.002 -25 1 -3 $ Air above mylar
14 7 -1.04 1 -4 10 -15 16 -21 24 25 $ Top ABS sheet
15 7 -1.04 8 -9 10 -15 16 -21 $ Bottom ABS sheet
16 7 -1.04 -24 1 -2 $ ABS filter above air
17 8 -1.00 28 -29 -30 $ Phantom
18 6 -.002 33 -31 -32 (-28:29:30) (-1:9:-10:15:-16:21) $ Air outside
19 0 -33:31:32
```


c Surface Descriptions

```

1 py 0
2 py .231
3 py .567
4 py .577
5 py .624
6 py .639
7 py .662
8 py .709
9 py .913
10 px 0
11 px .706
12 px 1.024
13 px 3.306
14 px 3.624
15 px 4.330
16 pz 0
17 pz .639
18 pz .957
19 pz 2.138
20 pz 2.456
21 pz 3.095
22 c/y .865 .798 .470
23 c/y .865 2.297 .470
24 c/y .865 2.297 .795
25 c/y 3.465 2.297 .470
26 c/y 3.465 .798 .470
27 py -201.27
28 py 1.413
29 py 11.913
30 c/y 2.165 1.5475 8
31 py 12
32 c/y 2.165 1.5475 9
33 py -202

```

c Cell Importances

MODE P

IMP:P 1 1 3 3 3 3 1 11R 0

c Photon Source Definition

SDEF POS=2.165 -201.27 1.5475 ERG=D1 SUR=27 RAD=D2 VEC 0 1 0 DIR=D3

SC1 ***** NIST H150 ENERGY SPECTRUM *****

```

SI1 .043 .044 .045 .046 .047 .048 .049 .050 .051 &
.052 .053 .054 .055 .056 .057 .058 .059 .060 .601 &
.062 .063 .064 .065 .066 .067 .068 .069 .070 .071 &
.072 .073 .074 .075 .076 .077 .078 .079 .080 .081 &
.082 .083 .084 .085 .086 .087 .088 .089 .090 .091 &
.092 .093 .094 .095 .096 .097 .098 .099 .100 .101 &
.102 .103 .104 .105 .106 .107 .108 .109 .110 .111 &
.112 .113 .114 .115 .116 .117 .118 .119 .120 .121 &
.122 .123 .124 .125 .126 .127 .128 .129 .130 .131 &
.132 .133 .134 .135 .136 .137 .138 .139 .140 .141 &
.142 .143 .144 .145 .146 .147 .148 .149
SP1 0 1 1 1 1 1 1 1 2 1 2 2 3 3 3 4 4 5 5 6 7 7 8 &
10 10 11 12 14 17 19 23 28 34 41 49 59 68 79 92 107 &
123 139 157 175 195 220 244 270 294 324 351 384 418 &
450 483 517 547 574 604 636 666 697 726 754 780 803 &
825 848 870 886 905 921 935 946 957 967 973 977 979 &
979 978 975 971 964 955 944 929 915 891 965 943 810 &
777 746 710 671 628 583 526 475 428 367 308 250 188 &

```

124 58
SC2 POSITION SAMPLING RADIAL DISTRIBUTION
SI2 0 2.54
SP2 -21 1
SC3 POLAR ANGLE SAMPLING DISTRIBUTION
SI3 .999928 1
SP3 -21 1
c Energy Deposition Tallies
FC18 ***** ENERGY DEPOSITION TALLY CHIP 1 *****
*F18:P 3
FC28 ***** ENERGY DEPOSITION TALLY CHIP 2 *****
*F28:P 4
FC38 ***** ENERGY DEPOSITION TALLY CHIP 3 *****
*F38:P 5
FC48 ***** ENERGY DEPOSITION TALLY CHIP 4 *****
*F48:P 6
c Material Compositions
M1 29000.02P 1
M2 1000.02P -.042 6000.02P -.625 8000.02P -.333
M3 3000.02P -.2704 9000.02P -.7296
M4 3000.02P -.2413 9000.02P -.7587
M5 13000.02P 1
M6 7000.02P -.755 8000.02P -.232 18000.02P -.013
M7 1000.02P -.089 6000.02P -.827 7000.02P -.084
M8 1000.02P -.08 6000.02P -.6 8000.02P -.32
NPS 30000000
PRINT

C.2 8825 Card Holder MCNP Input File

```

c 8825 CARD HOLDER
c Cell Descriptions
1 1 -8.96 -24 3 -5 $ Cu
2 2 -1.45 -26 4 -5 $ Mylar
3 3 -7.30 -27 2 -5 $ Sn
4 4 -2.63 7 -9 13 -14 21 -22 $ Chip 1
5 4 -2.63 7 -9 13 -14 19 -20 $ Chip 2
6 4 -2.63 7 -8 15 -16 19 -20 $ Chip 3
7 5 -2.63 7 -9 15 -16 21 -22 $ Chip 4
8 6 -2.669 24 25 26 27 6 -10 12 -17 18 -23 $ Al
9 7 -.002 -24 5 -10 (-7:9:-13:14:-21:22) $ Chip 1 Air
10 7 -.002 -25 5 -10 (-7:9:-13:14:-19:20) $ Chip 2 Air
11 7 -.002 -26 5 -10 (-7:8:-15:16:-19:20) $ Chip 3 Air
12 7 -.002 -27 5 -10 (-7:9:-15:16:-21:22) $ Chip 4 Air
13 7 -.002 -26 1 -4 $ Air IFO Mylar
14 8 -1.04 24 25 26 27 1 -6 12 -17 18 -23 $ Top ABS sheet
15 8 -1.04 -24 1 -3 $ ABS IFO Cu
16 10 -2.08 -25 1 -5 $ PTFE ifo Chip 2
17 8 -1.04 -27 1 -2 $ ABS IFO Sn
18 8 -1.04 10 -11 12 -17 18 -23 $ Bot ABS sheet
19 8 -1.04 -28 35 -1 $ ABS shell
20 9 -1.00 -31 11 -30 $ Tissue equiv. Phantom
21 7 -.002 -33 34 -32 (31:-11:30) (11:-1:-12:17:-18:23) (28:1)
22 0 33:32:-34
23 10 -2.08 -35 -1 $ PTFE Dome

```

```

c Surface Descriptions
1 py 0
2 py .1966
3 py .2448
4 py .2502
5 py .2550
6 py .436
7 py .483
8 py .4982
9 py .5211
10 py .568
11 py .735
12 px 0
13 px .706
14 px 1.024
15 px 3.306
16 px 3.624
17 px 4.330
18 pz 0
19 pz .639
20 pz .957
21 pz 2.138
22 pz 2.456
23 pz 3.095
24 c/y .865 2.297 .470
25 c/y .865 .798 .470
26 c/y 3.465 .798 .470
27 c/y 3.465 2.297 .470
28 s .865 .668 .798 .932
29 py -201.95

```

30 py 11.235
 31 c/y 2.165 1.5475 8
 32 py 11.5
 33 c/y 2.165 1.5475 9
 34 py -202
 35 s .865 .668 .798 .868

c Cell Importances

MODE P

IMP:P 1 1 1 3 3 3 3 1 13R 0 1

c Photon Source Definition

SDEF POS=2.165 -201.27 1.5475 ERG=D1 SUR=29 RAD=D2 VEC 0 1 0 DIR=D3

SC1 ***** NIST M60 ENERGY SPECTRUM *****

SI1 .0075 .0080 .0085 .0090 .0095 .0100 .0105 .0110 .0115 &
 .0120 .0125 .0130 .0135 .0140 .0145 .0150 .0155 .0160 .0165 &
 .0170 .0175 .0180 .0185 .0190 .0195 .0200 .0205 .0210 .0215 &
 .0220 .0225 .0230 .0235 .0240 .0245 .0250 .0255 .0260 .0265 &
 .0270 .0275 .0280 .0285 .0290 .0295 .0300 .0305 .0310 .0315 &
 .0320 .0325 .0330 .0335 .0340 .0345 .0350 .0355 .0360 .0365 &
 .0370 .0375 .0380 .0385 .0390 .0395 .0400 .0405 .0410 .0415 &
 .0420 .0425 .0430 .0435 .0440 .0445 .0450 .0455 .0460 .0465 &
 .0470 .0475 .0480 .0485 .0490 .0495 .0500 .0505 .0510 .0515 &
 .0520 .0525 .0530 .0535 .0540 .0545 .0550 .0555 .0560 .0565 &
 .0570 .0575 .0580 .0585 .0590 .0595 .0600

SP1 0 1 2 2 3 3 4 4 6 9 12 17 24 38 53 73 95 123 163 203 &
 254 303 358 409 452 496 543 587 638 677 713 751 784 815 844 &
 868 888 907 925 941 953 961 967 971 971 970 969 964 958 951 &
 942 930 921 908 897 885 874 859 846 830 814 799 784 767 752 &
 735 719 702 685 670 653 635 618 601 584 568 553 534 518 500 &
 482 468 450 432 413 396 378 362 345 326 306 289 273 256 236 &
 216 197 178 158 139 119 98 77 51 29 3

SC2 ***** POSITION SAMPLING RADIAL DISTRIBUTION *****

SI2 0 2.54

SP2 -21 1

SC3 ***** POLAR ANGLE SAMPLING DISTRIBUTION *****

SI3 .9997 1

SP3 -21 1

c Energy Deposition Tallies

FC18 ***** ENERGY DEPOSITION TALLY CHIP #1 *****

*F18:P 4

FC28 ***** ENERGY DEPOSITION TALLY CHIP #2 *****

*F28:P 5

FC38 ***** ENERGY DEPOSITION TALLY CHIP #3 *****

*F38:P 6

FC48 ***** ENERGY DEPOSITION TALLY CHIP #4 *****

*F48:P 7

c Material Compositions

M1 29000.02P 1

M2 1000.02P -.042 6000.02P -.625 8000.02P -.333

M3 50000.02P 1

M4 3000.02P -.2704 9000.02P -.7296

M5 3000.02P -.2413 9000.02P -.7587

M6 13000.02P 1

M7 7000.02P -.755 8000.02P -.232 18000.02P -.013

M8 1000.02P -.089 6000.02P -.827 7000.02P -.084

M9 1000.02P -.08 6000.02P -.6 8000.02P -.32

M10 6000.02P -.240 9000.02P -.760

NPS 50000000

PRINT

C.3 8825I Card Holder MCNP Input File

c 8825I CARD HOLDER

c Cell Descriptions

```

1 1 -8.96 -24 3 -36 $ Cu
2 2 -1.45 -26 4 -5 $ Mylar
3 3 -7.30 -27 2 -37 $ Sn
4 4 -2.63 7 -9 13 -14 21 -22 $ Chip 1
5 4 -2.63 7 -9 13 -14 19 -20 $ Chip 2
6 4 -2.63 7 -8 15 -16 19 -20 $ Chip 3
7 5 -2.63 7 -9 15 -16 21 -22 $ Chip 4
8 6 -2.669 24 25 26 27 6 -10 12 -17 18 -23 $ Al
9 7 -.002 -24 36 -10 (-7:9:-13:14:-21:22) $ Chip 1 Air
10 7 -.002 -25 5 -10 (-7:9:-13:14:-19:20) $ Chip 2 Air
11 7 -.002 -26 5 -10 (-7:8:-15:16:-19:20) $ Chip 3 Air
12 7 -.002 -27 37 -10 (-7:9:-15:16:-21:22) $ Chip 4 Air
13 7 -.002 -26 1 -4 $ Air IFO Mylar
14 8 -1.04 24 25 26 27 1 -6 12 -17 18 -23 $ Top ABS sheet
15 8 -1.04 -24 1 -3 $ ABS IFO Cu
16 10 -2.08 -25 1 -5 $ PTFE ifo Chip 2
17 8 -1.04 -27 1 -2 $ ABS IFO Sn
18 8 -1.04 10 -11 12 -17 18 -23 $ Bot ABS sheet
19 8 -1.04 -28 35 -1 $ ABS shell
20 9 -1.00 -31 11 -30 $ Tissue equiv. Phantom
21 7 -.002 -33 34 -32 (31:-11:30) (11:-1:-12:17:-18:23) (28:1)
22 0 33:32:-34
23 10 -2.08 -35 -1 $ PTFE Dome

```

c Surface Descriptions

```

1 py 0
2 py .1270
3 py .0635
4 py .2502
5 py .2550
6 py .436
7 py .483
8 py .4982
9 py .5211
10 py .568
11 py .735
12 px 0
13 px .706
14 px 1.024
15 px 3.306
16 px 3.624
17 px 4.330
18 pz 0
19 pz .639
20 pz .957
21 pz 2.138
22 pz 2.456
23 pz 3.095
24 c/y .865 2.297 .470
25 c/y .865 .798 .470
26 c/y 3.465 .798 .470
27 c/y 3.465 2.297 .470
28 s .865 .668 .798 .932
29 py -201.95

```

30 py 11.235
 31 c/y 2.165 1.5475 8
 32 py 11.5
 33 c/y 2.165 1.5475 9
 34 py -202
 35 s .865 .668 .798 .868
 36 py .2165
 37 py .2438

c Cell Importances

MODE P

IMP:P 1 1 1 3 3 3 3 1 13R 0 1

c Photon Source Definition

SDEF POS=2.165 -201.27 1.5475 ERG=D1 SUR=29 RAD=D2 VEC 0 1 0 DIR=D3

SC1 ***** NIST H60 ENERGY SPECTRUM *****

SI1 .0245 .025 .0255 .026 .0265 .027 .0275 .028 .0285 .029 &
 .0295 .03 .0305 .031 .0315 .032 .0325 .033 .0335 .034 .0345 &
 .035 .0355 .036 .0365 .037 .0375 .038 .0385 .039 .0395 .04 &
 .0405 .041 .0415 .042 .0425 .043 .0435 .044 .0445 .045 .0455 &
 .046 .0465 .047 .0475 .048 .0485 .049 .0495 .05 .0505 .051 &
 .0515 .052 .0525 .053 .0535 .054 .0545 .055 .0555 .056 .0565 &
 .057 .0575 .058 .0585 .059 .0595 .06

SP1 0 38 83 95 127 165 199 251 320 438 546 738 969 1206 &
 1581 1910 2299 2804 3465 4032 4757 5574 6321 7248 8223 9238 &
 10342 11274 12378 13411 14755 15830 17143 18168 19322 20403 &
 21599 22852 23641 24488 25106 26173 26811 27657 28217 28485 &
 29106 29248 29339 29375 29504 29277 28992 28621 28074 27339 &
 26690 25804 24820 23767 22406 20873 19439 17485 15730 13661 &
 11333 8841 5741 2825 852 176

SC2 ***** POSITION SAMPLING RADIAL DISTRIBUTION *****

SI2 0 2.54

SP2 -21 1

SC3 ***** POLAR ANGLE SAMPLING DISTRIBUTION *****

SI3 .9997 1

SP3 -21 1

c Energy Deposition Tallies

FC18 ***** ENERGY DEPOSITION TALLY CHIP #1 *****

*F18:P 4

FC28 ***** ENERGY DEPOSITION TALLY CHIP #2 *****

*F28:P 5

FC38 ***** ENERGY DEPOSITION TALLY CHIP #3 *****

*F38:P 6

FC48 ***** ENERGY DEPOSITION TALLY CHIP #4 *****

*F48:P 7

c Material Compositions

M1 29000.02P 1

M2 1000.02P -.042 6000.02P -.625 8000.02P -.333

M3 50000.02P 1

M4 3000.02P -.2704 9000.02P -.7296

M5 3000.02P -.2413 9000.02P -.7587

M6 13000.02P 1

M7 7000.02P -.755 8000.02P -.232 18000.02P -.013

M8 1000.02P -.089 6000.02P -.827 7000.02P -.084

M9 1000.02P -.08 6000.02P -.6 8000.02P -.32

M10 6000.02P -.240 9000.02P -.760

NPS 50000000

PRINT